Electrochimica Acta 296 (2019) 1142–1162

Contents lists available at ScienceDirect

Electrochimica Acta

journal homepage: www.elsevier.com/locate/electacta

Electrochemical-mechanical modeling of solid polymer electrolytes: Stress development and non-uniform electric current density in trench geometry microbatteries

Davide Grazioli [a, *], Vahur Zadin [b], Daniel Brandell [c], Angelo Simone [d, a]

[a] Faculty of Civil Engineering and Geosciences, Delft University of Technology, Stevinweg 1, 2628 CN Delft, the Netherlands
[b] IMS Lab, Institute of Technology, University of Tartu, Nooruse 1, 50411 Tartu, Estonia
[c] Department of Chemistry, Ångström Laboratory, Box 538, Uppsala University, 751 21 Uppsala, Sweden
[d] Department of Industrial Engineering, University of Padova, Via Venezia 1, 35131 Padua, Italy

ARTICLE INFO

Article history:
Received 24 April 2018
Received in revised form
19 July 2018
Accepted 20 July 2018
Available online 4 August 2018

Keywords:
Solid polymer electrolytes
Electrochemical-mechanical coupling
Trench geometry microbattery
Battery performance
Non-uniform electric current density

ABSTRACT

We study the effect of mechanical stresses arising in solid polymer electrolytes (SPEs) on the electrochemical performance of lithium-ion (Li-ion) solid-state batteries. Time-dependent finite element analyses of interdigitated plate cells during a discharge process are performed with a constitutive model that couples ionic conduction within the SPE with its deformation field. Due to the coupled nature of the processes taking place in the SPE, the non-uniform ionic concentration profiles that develop during the discharge process induce stresses and deformations within the SPE; at the same time the mechanical loads applied to the cell affect the charge conduction path. Results of a parametric study show that stresses induced by ionic redistribution favor ionic transport and enhance cell conductivity—up to a 15% increase compared to the solution obtained with a purely electrochemical model.

We observe that, when the contribution of the mechanical stresses is included in the simulations, the localization of the electric current density at the top of the electrode plates is more pronounced compared to the purely electrochemical model. This suggests that electrode utilization, a limiting factor for the design of three-dimensional battery architectures, depends on the stress field that develops in the SPE. The stress level is indeed significant, and mechanical failure of the polymer might occur during service.

© 2018 The Authors. Published by Elsevier Ltd. This is an open access article under the CC BY-NC-ND license (http://creativecommons.org/licenses/by-nc-nd/4.0/).

1. Introduction

Solid polymer electrolytes (SPEs) represent an attractive alternative to liquid electrolytes for lithium-ion (Li-ion) battery applications as they show enhanced resistance to variations in the volume of the electrodes, improved safety features, excellent flexibility and processability [1]. Being the polymer electrolyte a solid, concerns about its structural integrity arise, as mechanical failure would strongly affect the performance of the entire battery. A prediction of the stresses induced by the solicitations expected during service is therefore required. Here we make use of a finite element implementation of a coupled electrochemical-mechanical constitutive model to evaluate the impact of stresses arising in a SPE employed in a microbattery with a trench geometry.

SPEs are suitable for applications in which a liquid electrolyte could hardly be employed (3-D architecture microbatteries [2,3] and structural batteries [4,5]). In the context of medical implants, where the limited mass and volume of a typical energy storage device need to guarantee high energy and power densities, 3-D microbatteries with minimal or no packaging represent an attractive option, and SPEs meet most of the requirements for these devices, i.e., safety [6], reduced risk of leakage, and the possibility of being cast in complex architectures [7]. Moreover, the intrinsic multifunctional nature of SPEs [8] makes them appealing for structural batteries: they can serve as both electrolyte and solid matrix in which fiber-like reinforcing components are located [5].

Irrespective of the specific application, SPEs undergo deformations during normal operating conditions, either caused by the redistribution of ions [9] or by the expansion/contraction of the

* Corresponding author.
E-mail addresses: d.grazioli@tudelft.nl (D. Grazioli), vahur.zadin@ut.ee (V. Zadin), daniel.brandell@kemi.uu.se (D. Brandell), angelo.simone@unipd.it, a.simone@tudelft.nl (A. Simone).

https://doi.org/10.1016/j.electacta.2018.07.146
0013-4686/© 2018 The Authors. Published by Elsevier Ltd. This is an open access article under the CC BY-NC-ND license (http://creativecommons.org/licenses/by-nc-nd/4.0/).

active materials [10]. External mechanical loads are either applied on structural batteries intended to work as integrated structural elements as well as on batteries that power medical implants. A pressure stress state can be experienced by body-implanted batteries that power pressure sensors [11] or by those used in combination with piezoelectric power generators to convert the state of motion of the human body [12] into electrical energy [13]. External mechanical solicitations represent sources of additional deformations that induce a stress field in the SPE and should be carefully accounted for when the battery is designed.

Three-dimensional microbatteries are expected to yield higher capacity compared to uniform planar cells thanks to the larger volume of active materials that a 3-D architecture allows to accommodate [2,3]. Despite these promising features, experimental studies show that capacity enhancement is limited or absent if the cell is not carefully designed [14,15]. One of the factors that greatly contributes to reduced cell efficiency is the non-homogeneous current density distribution throughout the cell. This issue was first raised in the computational study performed by Hart et al. [16] on 3-D microbatteries, where it was shown that current density distribution is affected by the arrangement of the electrodes. The investigation carried by Zadin et al. [17–19] by means of finite element (FE) simulations further emphasizes the dependence of the charge conduction path on geometry and material properties of the battery components and shows that a non-homogeneous current density leads to a non-uniform utilization of the active material and to partially unexploited electrodes.

Numerical simulations provide insights on processes taking place in batteries during service without restrictions on the complexity of the battery architecture, allowing to explore conditions that could hardly be analyzed in experiments [10]. To this end, finite element simulations have been extensively employed to study electrochemical processes in 3-D microbatteries considering either liquid [16–18] or solid polymer [19–22] electrolytes. A vast literature exists on the modeling of electrochemical-mechanical interaction in Li-ion battery materials and components, either based on liquid or solid electrolytes [23]. Although mechanical stresses in solid-state batteries are known to impact on the electrical performance of the cell [10,24], numerical studies quantifying the stresses induced by a non-homogeneous current density [16] and the impact they have on the electrical response of the cell are not available for SPE-based 3-D microbatteries. The aim of this contribution is to fill this gap.

The SPE is regarded as a linear elastic material [9,10,24] in which transport of ionic species obeys the Nernst-Plank's equation. The latter is modified to account for the effect exerted by pressure gradients, and the kinematics is enriched to account for the deformation field induced by ionic redistribution. In agreement with the motivations provided in a companion paper [25], the coupling between electrochemical and mechanical fields is controlled by the partial molar volume of the ionic species resulting from the dissolution of lithium salt into the solid electrolyte. Boundary conditions are applied on current collectors, and the electrodes are included in the model. Even if the description of the processes in the electrolyte is our main focus, a realistic prediction of the charge conduction path cannot exclude the modeling of the electrodes. The latter is based on Ohm's law of electronic conduction (lithium diffusion and the resulting swelling and shrinkage are not considered) and the electrode-SPE interface is assumed to be perfect. These are the minimum requirements to determine the ionic concentration and electrostatic potential profiles within the SPE [18,19]. As discussed in Section 4, the electrodes are regarded as rigid bodies.

Two performance indicators are presented in Section 3 to evaluate the electrical battery response: cell conductivity and uniformity index. The first indicator quantifies the conductivity of the entire cell by providing an indirect evaluation of the effect of different factors (e.g., material properties and boundary conditions) on the ionic transport in the SPE material. The second provides a measure of the level of homogeneity of the electrode usage during charge/discharge processes, which is known to be an issue limiting the full exploitation of batteries based on 3-D architectures [14–20].

The model described in Section 2.1 is implemented in a finite element framework. Simulations are performed on microbatteries with a trench geometry (or 3-D microbatteries “trench” geometry [18,20]). The results indicate cell conductivity enhancement for increasingly large Young's modulus values of the polymer. The extent of the improvement relates to the geometrical features, up to 15% with respect to the purely electrochemical solution, and applies to stress-free and stressed batteries, as discussed in Section 4. The local enhancement of the ionic conduction mechanism induced by the stress field is however confined to regions where the pressure gradient is more pronounced. The results show that the deviation of the electrode utilization from the ideal uniform condition is proportional to the level of stresses attained in the electrolyte. The stress profiles reported in Section 4 show that the solicitations induced by the SPE swelling/shrinkage are beyond the elastic limit, indicating that the SPE will experience damage during regular discharge processes. It is shown that smoother battery geometries help reducing charge and stress localization, and the risk of mechanical failure in turn.

2. Model formulation

The battery cell is considered as a whole. Boundary conditions are applied at the electrode-current collector interface, Fig. 1, while specific boundary conditions for the electrolyte are determined by considering the interaction with the adjacent electrodes as detailed in Section 2.2. Current collectors are not modeled.

The following simplifying assumptions are considered:

1. the SPE is regarded as a homogeneous solid material in perfect contact with the electrodes;
2. electrical double layers at the electrode-electrolyte interface are not described;
3. side reactions are neglected in the whole cell;
4. saturation of the electrolyte is not accounted for;
5. the mechanical model, based on the infinitesimal strain theory, is applied to the solid polymer electrolyte only, and the volume changes of the electrodes are therefore neglected;
6. a linear elastic constitutive model is used for the mechanical description of the SPE [10,24,26];
7. the electrodes are regarded as solid and non-porous;
8. mass transport in the electrodes is not modeled and the state of charge in the electrodes is therefore assumed not to affect the current density in the battery [18,19]; and
9. the electrodes are regarded as rigid bodies because of their stiffness, largely exceeding that of the solid electrolyte as discussed in Section 4.

The formulation, as presented, applies to binary ionic compounds that dissociates into monovalent ions only (e.g., $LiPF_6$). Being the description of the processes in the electrolyte the main focus of this contribution, the insertion/extraction reactions at the electrodes are assumed not to contribute to the overall reaction rates, and the charge transport kinetics and mass transport in the electrodes are assumed not to affect the battery operations. Following the approach pursued in Refs. [18,19], we focus on the non-constant part of the electrostatic potential. The flux of the ionic species in the solid electrolyte is described through the Nernst-

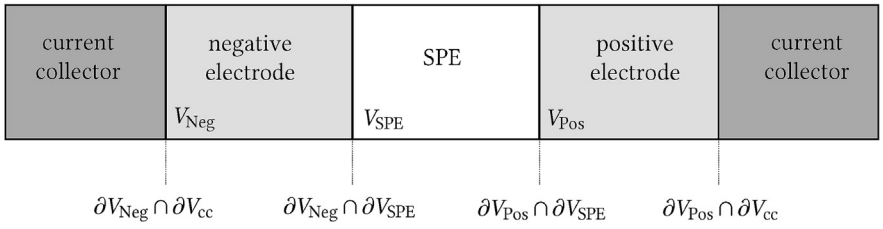

Fig. 1. Schematic of a battery cell.

Plank's equation [19] modified according to Refs. [9,24] to account for the effect of mechanical stresses.

2.1. Governing equations

The equations that govern the problem together with the interface conditions that define the interactions between cell components are summarized in this section. In what follows, the subscripts Pos, Neg and SPE refer to the positive and negative electrodes and to the solid polymer electrolyte, respectively. Likewise, the corresponding domain of validity of the constitutive equations are indicated with $\boldsymbol{x} \in V_k$, where $k =$ Pos, Neg or SPE. Throughout the text, bold small characters identify vectors, and bold capital or Greek characters identify tensors.

The modeling of the electrodes is limited to the charge conservation equation for conductive materials:

$$\operatorname{div} \boldsymbol{j}_{\mathrm{el}} = 0 \,.$$

By adopting Ohm's law to describe the electric current density,

$$\boldsymbol{j}_{\mathrm{el}} = -\kappa_{\mathrm{el}} \nabla\phi, \quad \boldsymbol{x} \in V_{\mathrm{el}}, \quad \mathrm{el} = \mathrm{Pos}, \mathrm{Neg}, \tag{1}$$

the governing equations for each electrode read:

$$\operatorname{div}(-\kappa_{\mathrm{Pos}} \nabla\phi) = 0 \,, \quad \boldsymbol{x} \in V_{\mathrm{Pos}}, \tag{2a}$$

$$\operatorname{div}(-\kappa_{\mathrm{Neg}} \nabla\phi) = 0 \,, \quad \boldsymbol{x} \in V_{\mathrm{Neg}}, \tag{2b}$$

where κ_j is the electronic conductivity (S m^{-1}) of the electrode j. The electrostatic potential ϕ is the only field variable related to the domains V_{Pos} and V_{Neg}.

Solid polymer electrolytes in lithium-ion batteries show a two-way coupling between electrochemistry and mechanics. The set of balance equations that govern the different physics involved in the SPE and the constitutive equations describing the electrochemical-mechanical coupling is thoroughly discussed in Ref. [25], where a set of governing equation formulated in terms of the electrostatic potential, positive and negative ions concentrations, and displacements was obtained. The electroneutrality condition was assumed to hold within the solid polymer electrolyte according to Ref. [19], so that the ionic concentrations, represented by the field variables c_{Li^+} and c_{X^-}, could be reduced to a single variable c according to

$$c_{\mathrm{Li}^+} = c_{\mathrm{X}^-} = c \,, \quad \boldsymbol{x} \in V_{\mathrm{SPE}} \,. \tag{3}$$

The electro-quasi-static form of Maxwell's equation could be used instead [27,28], but the electroneutrality condition is preferred because it allows to reduce the number of field variables while leading to the same results in terms of ionic concentration and electrostatic potential [27,29]. The electric current density $\boldsymbol{j}$ and the apparent mass flux $\boldsymbol{h}$ in the SPE can thus be written in terms of the gradients of the concentration c, electrostatic potential ϕ, pressure p, and the concentration itself:

$$\boldsymbol{j} = \gamma_c \nabla c - \gamma_\phi \, c \nabla\phi + \gamma_p \, c \nabla p \,, \quad \boldsymbol{x} \in V_{\mathrm{SPE}}, \tag{4}$$

$$\boldsymbol{h} = - D \nabla c - \frac{1}{2} \frac{D}{RT} \Omega \, c \nabla p, \quad \boldsymbol{x} \in V_{\mathrm{SPE}} \,. \tag{5}$$

Material parameters are collected into apparent diffusivity

$$D = \frac{2 \, D_{\mathrm{Li}^+} D_{\mathrm{X}^-}}{D_{\mathrm{Li}^+} + D_{\mathrm{X}^-}}, \tag{6}$$

combined partial molar volume

$$\Omega = \Omega_{\mathrm{Li}^+} + \Omega_{\mathrm{X}^-} \,, \tag{7}$$

and coefficients

$$\gamma_c = F \, (D_{\mathrm{X}^-} - D_{\mathrm{Li}^+}), \tag{8a}$$

$$\gamma_\phi = \frac{F^2}{RT} \, (D_{\mathrm{Li}^+} + D_{\mathrm{X}^-}), \tag{8b}$$

$$\gamma_p = F \, \frac{D_{\mathrm{X}^-}}{RT} \, \Omega \left(\frac{\Omega_{\mathrm{X}^-}}{\Omega} - \frac{D_{\mathrm{Li}^+}}{D_{\mathrm{X}^-}} \left(1 - \frac{\Omega_{\mathrm{X}^-}}{\Omega} \right) \right), \tag{8c}$$

where $F = 96485.3$ C mol^{-1} is the Faraday's constant, $R = 8.31447$ J K^{-1} mol^{-1} is the ideal gas constant, and T is the absolute temperature, taken as the room temperature ($T = 298.15$ K) in this study.

In line with the companion paper [25], the governing equations for the SPE are rephrased in a simplified form similar to what done in Refs. [19,29], but with the inclusion of the mechanical contribution. The balances of charge, mass and linear momentum are solved in a system of coupled equations written in terms of electrostatic potential ϕ, concentration c, displacement vector $\boldsymbol{u}$ and pressure p:

$$\operatorname{div}\left(\gamma_c \nabla c - \gamma_\phi \, c \nabla\phi + \gamma_p \, c \nabla p \right) = 0, \tag{9a}$$

$$\frac{\partial c}{\partial t} + \operatorname{div}\left(- D \nabla c - \frac{1}{2} \frac{D}{R\,T} \Omega \, c \nabla p \right) = 0, \tag{9b}$$

$$\operatorname{div}\left(2G \operatorname{dev} \boldsymbol{\varepsilon} + K \operatorname{tr} \boldsymbol{\varepsilon} \, \mathbf{1} - K \, \Omega \left(c - c^0 \right) \mathbf{1} \right) = 0, \tag{9c}$$

$$p = - K \operatorname{tr} \boldsymbol{\varepsilon} + K \, \Omega \left(c - c^0 \right), \tag{9d}$$

with $\boldsymbol{x} \in V_{\mathrm{SPE}}$. The pressure term is explicitly introduced into the system of equations for implementation convenience (refer to Appendix A for details). The strain tensor

Table 1
Summary of the governing equations that follow from the electroneutrality assumption.

	V_{Neg}	V_{SPE}	V_{Pos}
Charge balance	$\text{div}(-\kappa_{\text{Neg}}\nabla\phi) = 0$	$\text{div}\left(\gamma_c \nabla c - \gamma_\phi c \nabla\phi + \gamma_p c \nabla p\right) = 0$	$\text{div}(-\kappa_{\text{Pos}}\nabla\phi) = 0$
Mass balance		$\frac{\partial c}{\partial t} + \text{div}\left(-D\nabla c - \frac{1}{2}\frac{D}{RT}\Omega c \nabla p\right) = 0$	
Balance of linear momentum		$\text{div}(2G\,\text{dev}\,\boldsymbol{\varepsilon} + K\,\text{tr}\,\boldsymbol{\varepsilon}\,\mathbf{1} - K\Omega(c-c^0)\mathbf{1}) = 0$	
Pressure		$p = -K\,\text{tr}\,\boldsymbol{\varepsilon} + K\Omega(c-c^0)$	

$$\boldsymbol{\varepsilon} = \frac{1}{2}\left(\nabla\boldsymbol{u} + \nabla\boldsymbol{u}^T\right), \quad \boldsymbol{x}\in V_{\text{SPE}} \tag{10}$$

is defined as usual. The electronic conductivities of the electrodes and the diffusion coefficients, partial molar volume, and mechanical properties of the solid polymer electrolyte appearing in (2), (6), (7), (8) and (9c) are assumed to be constant. The governing equations are summarized in Table 1, while the values used in the numerical simulations are listed in Table 3.

2.2. Interface conditions

We assume that battery operations are limited neither by mass transport in active material nor by electrode kinetics and that the electrodes are characterized by a uniform lithium concentration distribution. We also assume that the open circuit potentials $V_{\text{OC}}^{\text{Pos}}$ and $V_{\text{OC}}^{\text{Neg}}$ associated with the positive and negative electrode, respectively, are uniform in space and constant in time. It follows that the surface overpotential is negligible. The electrostatic potential at the two sides of the interface are thus related through

$$\phi_{\text{Pos}} - \phi_{\text{SPE}} = V_{\text{OC}}^{\text{Pos}}, \quad \boldsymbol{x}\in\partial V_{\text{Pos}}\cap\partial V_{\text{SPE}}, \tag{11a}$$

$$\phi_{\text{Neg}} - \phi_{\text{SPE}} = V_{\text{OC}}^{\text{Neg}}, \quad \boldsymbol{x}\in\partial V_{\text{Neg}}\cap\partial V_{\text{SPE}}, \tag{11b}$$

where ∂V denotes the boundary of domain V and the subscripts, omitted in the previous section, indicate which side of the interface the variables refer to. Since $V_{\text{OC}}^{\text{Pos}}$ and $V_{\text{OC}}^{\text{Neg}}$ are uniform within each electrode, they have vanishing gradients and do not affect the electric current density distribution (1).

Continuity of the electric current density across the electrode-electrolyte interface is enforced through

$$-\boldsymbol{j}_{\text{Pos}}\cdot\boldsymbol{n}_{\text{Pos}} = \boldsymbol{j}_{\text{SPE}}\cdot\boldsymbol{n}_{\text{SPE}} = j_{\text{Pos}}, \quad \boldsymbol{x}\in\partial V_{\text{Pos}}\cap\partial V_{\text{SPE}}, \tag{12a}$$

$$\boldsymbol{j}_{\text{Neg}}\cdot\boldsymbol{n}_{\text{Neg}} = -\boldsymbol{j}_{\text{SPE}}\cdot\boldsymbol{n}_{\text{SPE}} = j_{\text{Neg}}, \quad \boldsymbol{x}\in\partial V_{\text{Neg}}\cap\partial V_{\text{SPE}}. \tag{12b}$$

According to the convention adopted, j_{Pos} and j_{Neg} are positive when the electric current flows from the SPE toward the electrode at the positive electrode-SPE boundary, and from the electrode towards the SPE at the negative electrode-SPE boundary, respectively.

Since the amount of lithium ions exchanged at the electrode-electrolyte interface during battery operations is related to the transferred electric charge, while the anionic mass flux is homogeneous across the interface, the following relation holds between apparent mass flux and electric current density [25]:

$$\boldsymbol{h}\cdot\boldsymbol{n}_{\text{SPE}} = \frac{1}{F}\frac{D_{\text{X}^-}}{D_{\text{Li}^+} + D_{\text{X}^-}}\boldsymbol{j}_{\text{SPE}}\cdot\boldsymbol{n}_{\text{SPE}},$$

$$\boldsymbol{x}\in(\partial V_{\text{Pos}}\cap\partial V_{\text{SPE}})\cup(\partial V_{\text{Neg}}\cap\partial V_{\text{SPE}}). \tag{13}$$

The mechanical response of the electrodes is not taken into account in the simulations, and the electrode-electrolyte interface is considered as a regular external boundary for the electrolyte. Their description is postponed to Section 4 where boundary conditions are discussed. Details about the implementation of the governing equations (2) and (9) and the interactions between battery components (11), (12) and (13) are reported in Appendix A.

Zadin et al. performed FE simulations of microbatteries with a trench geometry with a purely electrochemical model by either enforcing condition (11) [18] or explicitly describing the interface reaction kinetic [17] through the Butler-Volmer equation [30] coupled with the diffusion taking place in the electrodes. The results obtained with the two approaches show that only the long-term response within a single discharge (charge) process of the system is affected by the electrode-electrolyte interface description. When the reaction kinetic is explicitly modeled [17], the ionic diffusion path in the electrolyte modifies in response to the depletion/saturation of specific regions of the electrodes surface where the charge and lithium extraction/insertion cannot take place anymore, i.e., $\boldsymbol{j}_{\text{SPE}}\cdot\boldsymbol{n}_{\text{SPE}}\approx 0$ and $\boldsymbol{h}\cdot\boldsymbol{n}_{\text{SPE}}\approx 0$.

Since the focus of this contribution is to highlight the effects of electrochemical-mechanical coupling on the performance of the battery cell, the electrode model (2) and the above mentioned simplifying assumption on $V_{\text{OC}}^{\text{Pos}}$ and $V_{\text{OC}}^{\text{Neg}}$ are used to limit the number of factors affecting the time-response of the system and to isolate the contribution of the stress field. A similar approach was adopted in previous studies where 2-D [18] and 3-D [19] numerical simulations on microbattery architectures were performed. Interface conditions are summarized in Table 2.

Table 2
Summary of the continuity conditions across each electrode-SPE interface.

$V_{\text{Neg}}\cap\partial V_{\text{SPE}}$	$\partial V_{\text{Pos}}\cap\partial V_{\text{SPE}}$
$\phi_{\text{Neg}} - \phi_{\text{SPE}} = V_{\text{OC}}^{\text{Neg}}$	$\phi_{\text{Pos}} - \phi_{\text{SPE}} = V_{\text{OC}}^{\text{Pos}}$
$\boldsymbol{j}_{\text{Neg}}\cdot\boldsymbol{n}_{\text{Neg}} = -\boldsymbol{j}_{\text{SPE}}\cdot\boldsymbol{n}_{\text{SPE}} = j_{\text{Neg}}$	$-\boldsymbol{j}_{\text{Pos}}\cdot\boldsymbol{n}_{\text{Pos}} = \boldsymbol{j}_{\text{SPE}}\cdot\boldsymbol{n}_{\text{SPE}} = j_{\text{Pos}}$
$\boldsymbol{h}\cdot\boldsymbol{n}_{\text{SPE}} = -\frac{1}{F}\frac{D_{\text{X}^-}}{D_{\text{Li}^+}+D_{\text{X}^-}}j_{\text{Neg}}$	$\boldsymbol{h}\cdot\boldsymbol{n}_{\text{SPE}} = \frac{1}{F}\frac{D_{\text{X}^-}}{D_{\text{Li}^+}+D_{\text{X}^-}}j_{\text{Pos}}$

3. Performance indicators

Previous numerical studies [18,19] discussed the influence of cell geometry and electric conductivity of the electrodes on ionic concentration and mass flux distributions within the electrolyte by adopting a model focused on the purely electrochemical contribution. Since the field variables were limited to ionic concentration and electrostatic potential [18], and time-independent processes were considered [19], only a qualitative comparison between the results obtained for different combination of geometrical features and material parameters was performed.

Table 3
Material parameters, geometrical features, initial and boundary conditions.

Symbol	Quantity	Value
κ_{LiCoO_2}	Electronic conductivity of $LiCoO_2$ [18]	1.0×10^{-2} Sm^{-1}
κ_{C_6}	Electronic conductivity of C_6 [18]	1.0 Sm^{-1}
D_{Li^+}	Diffusion constant for Li^+ ions in SPE [19]	2.5×10^{-13} m^2 s^{-1}
$D_{PF_6^-}$	Diffusion constant for PF_6^- ions in SPE [19]	3.0×10^{-13} m^2 s^{-1}
E	Young's modulus of the SPE [34–38]	5, 50, 140, 500 MPa
ν	Poisson's ratio of the SPE [35]	0.24
Ω	Combined partial molar volume of $LiPF_6$ in SPE[a]	1.1×10^{-4}, 1.5×10^{-4} m^3 mol^{-1}
$\Omega_{PF_6^-}/\Omega$	Contribution of PF_6^- to the combined partial molar volume[a]	37/38
h	Height of the trench	25, 50, 75 μm
r	Corner tip radius of the trench	1, 5 μm
c^0	Salt concentration in the SPE [19]	1500 mol m^{-3}
ΔV_{disc}	Applied potential difference	− 0.1 V
Δu	Applied displacement	0, 0.25, 0.5, 1 μm

[a] Refer to [25] for details.

The adoption of scalar performance indicators becomes unavoidable for parametric studies in which different geometries, material parameters and boundary conditions are examined—scalar quantities are more convenient to deal with and make comparisons immediate. Two time-dependent scalar performance indicators are selected to monitor a specific feature of the cell. As discussed in the following sections, the set of parameters that determines improved performance according to one of them may cause the reduction of performance according to the other.

3.1. Cell conductivity

Although the use of solid polymer electrolytes for 3-D microbatteries presents several advantages with respect to their liquid counterpart, the low ionic conductivity poses obstacles to their application in high power micro-devices that require high electric currents [2]. Experimental studies report further reduction of the ionic conductivity for SPEs characterized by increasingly high values of the stiffness [31]. Despite these discouraging material level observations, a different trend holds at the cell level. Provided that the electrochemical properties of the SPE are unchanged, modification of the SPE stiffness can determine either an increase or a decrease of the overall ionic conduction depending on the geometrical features of the cell as shown in Section 4.

The cell conductivity

$$\overline{\kappa} = \frac{\bar{j}}{\Delta\overline{V}} \tag{14}$$

is chosen as performance indicator. The quantity

$$\Delta\overline{V} = |\Delta V_{proc} - \Delta V_{OC}| \tag{15}$$

is the absolute value of the cell overpotential averaged over the contact surfaces between the electrodes and the current collectors, Fig. 1,

$$\Delta V_{proc} = \frac{1}{\overline{S}}\int_{\partial V_{Pos}\cap\partial V_{cc}} \phi_{Pos}\, dS - \frac{1}{\overline{S}}\int_{\partial V_{Neg}\cap\partial V_{cc}} \phi_{Neg}\, dS \tag{16}$$

is the potential difference related to the process (charge or discharge),

$$\Delta V_{OC} = V_{OC}^{Pos} - V_{OC}^{Neg} \tag{17}$$

is the cell open circuit potential, and

$$\bar{j} = \frac{1}{\overline{S}}\left|\int_{\partial V_{el}\cap\partial V_{cc}} \boldsymbol{j}_{el}\cdot\boldsymbol{n}_{el}\, dS\right| \tag{18}$$

is the average electric current density flowing through the cell. Subscript el identifies either the positive, el = Pos, or the negative, el = Neg, electrode, and $\boldsymbol{n}_{el}$ represents the unit vector normal to the contact surface pointing from the electrode toward the current collector. Because of charge conservation, the integral in (18) assumes the same value at $\partial V_{Pos}\cap\partial V_{cc}$ and $\partial V_{Neg}\cap\partial V_{cc}$ at every instant of time and for any process, provided that the extension of the contact surfaces

$$\overline{S} = \int_{\partial V_{el}\cap\partial V_{cc}} dS \tag{19}$$

is equal in the positive and negative electrode. This is always the case for the battery architectures dealt with in this contribution.

Since the ionic conduction depends on the pressure gradient, a relation is found between the stress field in the SPE and measurable quantities such as the electric current flowing through the cell and the electrostatic potential difference across the electrodes. This makes the cell conductivity suitable for comparison with experiments. The cell conductivity just introduced coincides with the inverse of the resistivity defined by Zadin et al. [20].

3.2. Uniformity index

Microbatteries cast in 3-D architectures potentially allow to combine high energy density and limited dimensions. However, the theoretical energy enhancement allowed by 3-D architectures is partially unexploited due to the underutilization of the material in the electrodes. The combined computational-experimental study conducted by Talin et al. [15] indicates the non-uniform electric current density distribution as one of the factors that limits the electrochemical performance of 3-D batteries. When comparing the capacity of batteries with planar and 3-D architectures, with the same material composition and comparable geometrical features, the authors observed better performance of the 3-D architectures at low externally applied currents, associated with an increased active volume available for storage. However, at slightly higher currents the capacity reduction for the 3-D architecture was dramatic but it was not equivalently observed in the planar cell. Talin et al. [15] ascribe this issue to the non-homogeneous electric current density within the cell and to the consequent non-uniform electrode utilization in the 3-D battery, in agreement with

previous numerical studies performed by Hart et al. [16] and Zadin et al. [17–19]. Similar arguments apply to the experimental observations reported by Cirigliano et al. [14] who, accounting for the non-homogeneous current density distributions predicted by Zadin et al.'s FE simulations [17–19], achieved an improved design for 3-D microbatteries.

An indication of the current distribution within the cell can be obtained by monitoring the electric current density profile along the electrode-electrolyte interface. Given the component of the electric current density along the interface in the direction transverse to it,

$$\boldsymbol{j}_{\mathrm{el}}\cdot\boldsymbol{n}_{\mathrm{el}}\,,\quad \boldsymbol{x}\in\partial V_{\mathrm{el}}\cap\partial V_{\mathrm{SPE}}\,,$$

the scalar

$$j_{\mathrm{diff}}=\sqrt{\frac{1}{\bar{S}_{\mathrm{int}}}\int_{\partial V_{\mathrm{el}}\cap\partial V_{\mathrm{SPE}}}\left(\left(\boldsymbol{j}_{\mathrm{ref}}-\boldsymbol{j}_{\mathrm{el}}\right)\cdot\boldsymbol{n}_{\mathrm{el}}\right)^2\,\mathrm{d}S} \tag{20}$$

is introduced to quantify the extent to which the electric current density profile deviates from a reference current density distribution $\boldsymbol{j}_{\mathrm{ref}}$ along the interface, with

$$\bar{S}_{\mathrm{int}}=\int_{\partial V_{\mathrm{el}}\cap\partial V_{\mathrm{SPE}}}\mathrm{d}S,\quad \mathrm{el}\;=\;\mathrm{Pos},\;\mathrm{Neg}, \tag{21}$$

the contact surface between electrode and electrolyte. A similar choice was made by Zhuang et al. [32] who used the quadratic temperature gradient as objective function in their geometry optimization process.

At each instant of time, the mean value $\bar{j}_{\mathrm{int}}$ of the electric current density transferred trough the electrode-SPE interface is defined as

$$\bar{j}_{\mathrm{int}}=\frac{1}{\bar{S}_{\mathrm{int}}}\left|\int_{\partial V_{\mathrm{el}}\,\cap\,\partial V_{\mathrm{SPE}}}\boldsymbol{j}_{\mathrm{el}}\cdot\boldsymbol{n}_{\mathrm{el}}\;\mathrm{d}S\right|. \tag{22}$$

Because of charge conservation, the integral assumes the same value at $\partial V_{\mathrm{Pos}}\cap\partial V_{\mathrm{SPE}}$ and $\partial V_{\mathrm{Neg}}\cap\partial V_{\mathrm{SPE}}$ (at any instant of time and for any process) if the extension of the contact surfaces $\bar{S}_{\mathrm{int}}$ is the same at this interface.

By selecting the reference electric current density so that its component aligned with the direction normal to the interface is uniform (independent of location along the interface) and satisfies

$$\boldsymbol{j}_{\mathrm{ref}}\cdot\boldsymbol{n}_{\mathrm{el}}\;=\;\bar{j}_{\mathrm{int}},\quad \boldsymbol{x}\in\partial V_{\mathrm{el}}\cap\partial V_{\mathrm{SPE}}, \tag{23}$$

and recalling the definitions of j_{Pos} and j_{Neg} (12), the scalar (20) is rephrased as

$$j_{\mathrm{diff}}=\sqrt{\frac{1}{\bar{S}_{\mathrm{int}}}\int_{\partial V_{\mathrm{el}}\,\cap\,\partial V_{\mathrm{SPE}}}j_{\mathrm{el}}^2\;\mathrm{d}S\;-\;\bar{j}_{\mathrm{int}}^2}\,. \tag{24}$$

For 3-D battery architectures, the orientation of the normal vector $\boldsymbol{n}_{\mathrm{el}}$ depends on the specific location along the interface but is constant in time due to the infinitesimal strain theory. Nevertheless, both $\bar{j}_{\mathrm{int}}$ and j_{diff} are time-dependent quantities due to their dependence from $\boldsymbol{j}_{\mathrm{el}}$.

The non-dimensional uniformity index

$$\mathrm{UI}=\frac{j_{\mathrm{diff}}}{\bar{j}_{\mathrm{int}}} \tag{25}$$

is selected as performance indicator. With reference to (22) and (24), the uniformity index is non-negative and equals zero if j_{el} is uniform along the interface. The closer UI to zero the more the current density approaches a uniform distribution along the interface.

4. Results and discussion

Numerical simulations of microbatteries with a trench geometry [2,17,18] are performed using the domain highlighted in Fig. 2a and described by means of the 2-D setting of Fig. 2b. Since the out-of-plane dimension exceeds the width of the SPE domain [33], plane strain conditions are assumed to hold for the mechanical contribution.

The materials considered for the positive and negative electrode are lithium cobalt oxide ($LiCoO_2$) and graphite (C_6), respectively, while the solid polymer electrolyte is a PEO with $LiPF_6$ salt. The material parameters used in the numerical analyses are listed in Table 3. Different values of the Young's modulus ($E=5$, 50, 140 and 500 MPa) are considered for the SPE to investigate its impact on the battery cell performance for a fixed set of electrochemical properties. This range is selected according to experimental studies carried either on PEO [34–36] or poly(propylene glycol) diacrylate (PPGDA) [37,38] which have structural similarities and show similar properties [39]. The electrodes are considered as rigid bodies because the characteristic Young's moduli of $LiCoO_2$ and C_6 are about 150 GPa [40–42] and 25 GPa [43,44], respectively, and they largely exceed the highest value used for the SPE. Similar to [25], the simulations are performed with $\Omega=1.1\times10^{-4}\,\mathrm{m^3\,mol^{-1}}$ and $1.5\times10^{-4}\,\mathrm{m^3\,mol^{-1}}$, and $\Omega_{PF_6^-}/\Omega=37/38$ is used to evaluate coefficient γ_p (8c).

Fig. 2b shows the geometry of the microbattery with the width $W=20\,\mu$m of the simulated domain, and the thickness $w=10\,\mu$m of the trenches and the SPE layer that separates the electrodes. The height of the trenches and of the domain are denoted with h and H, respectively, and the radius of curvature at the tip and foot of the trenches with r. Different cell geometries, resulting from the combination of $h=25$, 50 and 75 μm and $r=1$ and 5 μm, are considered in the simulations.

Triangular linear elements are used in the FE simulations. The meshes are refined until convergence is achieved for the average electric current density (18) and the uniformity index (25). The results in this section are obtained with a number of elements comprised between 16000 and 33500, depending on the cell geometry. The edge of the average element is shorter than 0.7 μm apart from the region in the proximity of the tip of the trenches where the element edge length was reduced to 0.2 μm. The time step is kept constant during the simulations. Due to negligible differences obtained with values between 1 and 10 s, the results in this section are obtained with a time step equal to 10 s.

A potentiostatic discharge process was simulated. For the sake of simplicity we chose $V_{\mathrm{OC}}^{\mathrm{Pos}}=V_{\mathrm{OC}}^{\mathrm{Neg}}=0$ (in view of the simplifying assumption taken and the arguments exposed in Section 2.2 this particular choice does not lead to modification of the electric current density distribution) and applied the potential difference $\Delta V_{\mathrm{disc}}=-0.1$ V between the electrodes after setting the negative electrode as reference:

$$\phi|_{y=0}=0,\quad \boldsymbol{x}\in V_{\mathrm{Neg}}, \tag{26a}$$

$$\phi|_{y=H}=\Delta V_{\mathrm{disc}},\quad \boldsymbol{x}\in V_{\mathrm{Pos}}\,. \tag{26b}$$

Due to symmetry, homogeneous Neumann boundary conditions are applied along the vertical edges of the domain for the electric current density:

$$\boldsymbol{j}_{\mathrm{Pos}}\cdot\boldsymbol{n}|_{x=0}=\boldsymbol{j}_{\mathrm{Pos}}\cdot\boldsymbol{n}|_{x=W}=0,\quad \boldsymbol{x}\in V_{\mathrm{Pos}}, \tag{27a}$$

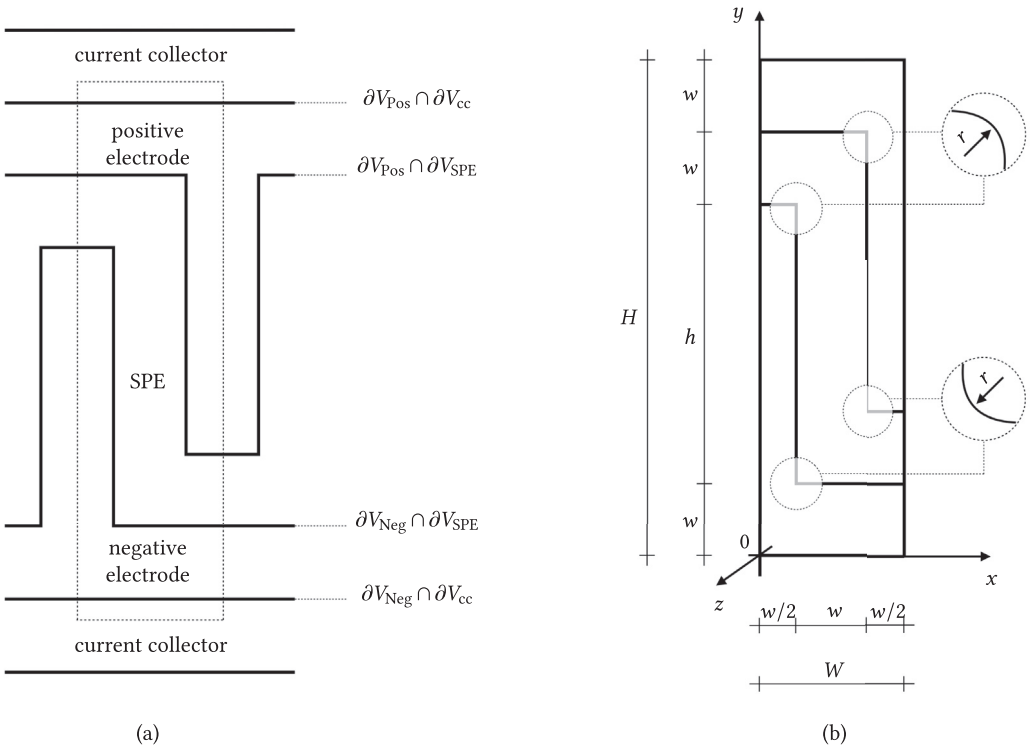

Fig. 2. Schematic of a microbattery with a trench geometry: (a) detail of the cell layout (pattern repeated several times in trench geometry microbatteries) with simulation domain enclosed in the dotted box, and (b) details of the simulation domain.

$$\boldsymbol{j}_{\mathrm{Neg}} \cdot \boldsymbol{n}|_{x=0} = \boldsymbol{j}_{\mathrm{Neg}} \cdot \boldsymbol{n}|_{x=W} = 0, \quad \boldsymbol{x} \in V_{\mathrm{Neg}}, \tag{27b}$$

$$\boldsymbol{j}_{\mathrm{SPE}} \cdot \boldsymbol{n}|_{x=0} = \boldsymbol{j}_{\mathrm{SPE}} \cdot \boldsymbol{n}|_{x=W} = 0, \quad \boldsymbol{x} \in V_{\mathrm{SPE}}, \tag{27c}$$

and for the mass flux:

$$\boldsymbol{h}_{\mathrm{SPE}} \cdot \boldsymbol{n}|_{x=0} = \boldsymbol{h}_{\mathrm{SPE}} \cdot \boldsymbol{n}|_{x=W} = 0, \quad \boldsymbol{x} \in V_{\mathrm{SPE}}\,. \tag{28}$$

The initial condition

$$c = c^0, \quad \boldsymbol{x} \in V_{\mathrm{SPE}},\ t = 0, \tag{29}$$

with $c^0 = 1500\ \mathrm{mol\ m^{-3}}$ [19], applies to the mass conservation equation (9b).

The SPE is in a stress-free state in the initial (undeformed) configuration according to definition (9d). By assuming perfect adhesion between polymer and electrodes (regarded as rigid bodies), the negative electrode-SPE interface is therefore regarded as fixed:

$$u_x = u_y = 0, \quad \boldsymbol{x} \in \partial V_{\mathrm{Neg}} \cap \partial V_{\mathrm{SPE}}\,. \tag{30}$$

Horizontal displacements are restricted according to

$$u_x = 0, \quad \boldsymbol{x} \in \partial V_{\mathrm{Pos}} \cap \partial V_{\mathrm{SPE}}, \tag{31a}$$

$$u_x|_{x=0} = u_x|_{x=W} = 0, \quad \forall \boldsymbol{x} \in V_{\mathrm{SPE}}, \tag{31b}$$

where (31a) accounts for the perfect adhesion between SPE and the positive electrode, while (31b) reflects the symmetry of the cell depicted in Fig. 2. Different values of the vertical displacement are applied on the positive electrode interface to investigate the effect of externally applied compressive mechanical loads enforced by means of the prescribed displacement

$$u_y = -\,\Delta u, \quad \boldsymbol{x} \in \partial V_{\mathrm{Pos}} \cap \partial V_{\mathrm{SPE}}\,. \tag{32}$$

In the framework of medical devices, this could be representative of batteries powering implantable pressure sensors placed in the pulmonary artery [11], or batteries coupled to piezoelectric power generator able to convert mechanical energy from body movement into electricity [13]. Due to their potential multifunctionality, implantable solid-state batteries should be able to withstand stresses and shocks which are, in traditional battery designs, withstood by the packaging [12].

The system of governing equations described in Section 2 does not account for the lithium depletion/saturation of the electrodes. With this setting, the discharge time interval $[0, t_{\mathrm{end}})$ has no upper bound as there are no constraints on the charge/lithium that can be transferred from one electrode to the other. To overcome this limitation, a realistic end time t_{end} is determined from the cell capacity C_{cell} for each battery geometry and obtained from the material properties of the positive electrode ($LiCoO_2$). A reversible specific capacity equal to 140 mAh g^{-1} is usually assigned to $LiCoO_2$ (see for example [45]), corresponding to half the theoretical value [46]. Assuming a density $\rho_{\mathrm{LiCoO_2}} \approx 5\ \mathrm{g\ cm^{-3}}$ [47], the capacity of the cell is determined as

$$C_{\mathrm{cell}} = 140\ \mathrm{mAh\ g^{-1}} \times \rho_{\mathrm{LiCoO_2}} \times A_{\mathrm{Pos}} \times 1\ \mu\mathrm{m}, \tag{33}$$

where $A_{\mathrm{Pos}} \times 1\ \mu$m is the volume occupied by the positive electrode, given by the product of the area A_{Pos} in the xy-plane in Fig. 2b, and factor 1 μm. The latter is included to emphasize that C_{cell} should otherwise be expressed per unit thickness (out of plane, z-axis). Values of C_{cell} for the domain represented in Fig. 2b are: 2.23×10^{-10} Ah for $h = 25\ \mu$m cell, 3.09×10^{-10} Ah for $h = 50\ \mu$m cell, and 3.94×10^{-10} Ah for $h = 75\ \mu$m cell. In all the simulations $t \in [0, t_{\mathrm{end}}]$ such that

$$\bar{S} \int_0^{t_{\mathrm{end}}} \bar{j}\, \mathrm{d}t = C_{\mathrm{cell}}\,. \tag{34}$$

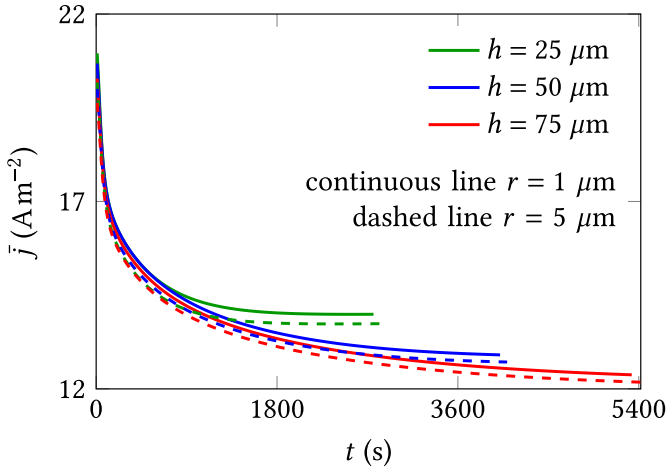

Fig. 3. Time evolution of the average electric current density (18). Simulations performed with the purely electrochemical model. The extent of the electric current density is inversely proportional to h and is higher for $r = 1$ μm than for $r = 5$ μm at any instant of time $t \in [0, t_{end}]$, irrespective of the height of the trenches.

Equation (34) provides a definition of t_{end} as the time required to discharge a fully charged cell.

4.1. Electrochemical model

The time evolution of the average current density (18) during the discharge process simulated without the mechanical contribution is reported in Fig. 3 for the battery geometries under investigation (in Fig. 3 and hereafter the same color is used for cells with trenches of the same eight h, while continuous and dashed lines are used for $r = 1$ μm and $r = 5$ μm, respectively). A common trend is apparent: the current density monotonically decreases from an initial value toward a plateau, reducing to about 0.65 times its initial value. This time-dependent behavior is typical of systems containing ionic conductors. A similar response is reported by Le Van-Jodin et al. [48] for an amorphous ionic conducting glass (LiPON) subject to a constant 0.5 V potential. At the beginning of the discharge process ($t = 0$), ions are uniformly distributed throughout the electrolyte and available for charge transport. A redistribution occurs afterwards and a non-uniform ionic concentration profile develops. The concentration gradient that builds up along the direction of the electric current flux shows a trend similar to that experimentally observed by Klett et al. [49], but with a two-dimensional pattern because of the cell geometry. Due to the redistribution, ions cover larger distances to ensure a continuous charge transfer, reducing the overall ionic conduction in the SPE and the cell current density. The average electric current density $\bar{j}$ approaches the steady state value at $t = t_{end}$ (the actual steady state is reached by the 25 μm high trench cell only, after roughly 2000 s). The steady state corresponds to the condition of the system at which no appreciable variations of the field variables occur, i.e., $\partial c/\partial t \approx 0$ for the set of governing equations described in Section 2. The steady state is achieved before the cell is fully discharged (for $t < t_{end}$) in two cases: 1) the evolution of the system is rapid, i.e., the characteristic time of the diffusion process is small compared to t_{end}; 2) the redistribution of concentration is limited. The second scenario is observed when the electrochemical-mechanical model is used, as the deviation of the concentration profile in the SPE from a uniform distribution is limited by the pressure contribution (Fig. 7).

The cell conductivity (14) is strongly influenced by the geometrical features of the battery, as different values of the electric current density correspond to the same applied potential difference ΔV_{disc}. Fig. 3 shows that the average electric current density is higher in batteries with shorter trenches and is maximum for batteries with 25 μm high trenches. Moreover, a current density reduction manifests when the radius r of the tip corners changes from 1 to 5 μm.

Fig. 4 reports the time evolution of the uniformity index (25) for both electrode-electrolyte interfaces. Two trends are apparent. First, the value of the uniformity index reduces in batteries with shorter trenches and with smoother corners at the tip, suggesting that the electric current density approaches a uniform distribution in cells whose geometry approaches that of a uniform planar cell (recall that according to (24) and (25) a uniform electric current distribution leads to UI $= 0$). Second, irrespective of the height and corner radius of the trenches, the values attained by the uniformity index along the $LiCoO_2$/SPE interface (Fig. 4a) are roughly half of those attained along the C_6/SPE interface (Fig. 4b). The different utilization of the two electrodes follows from the higher electronic conductivity of graphite with respect to the $LiCoO_2$, forcing the electronic current to pass mainly through the negative electrode tip

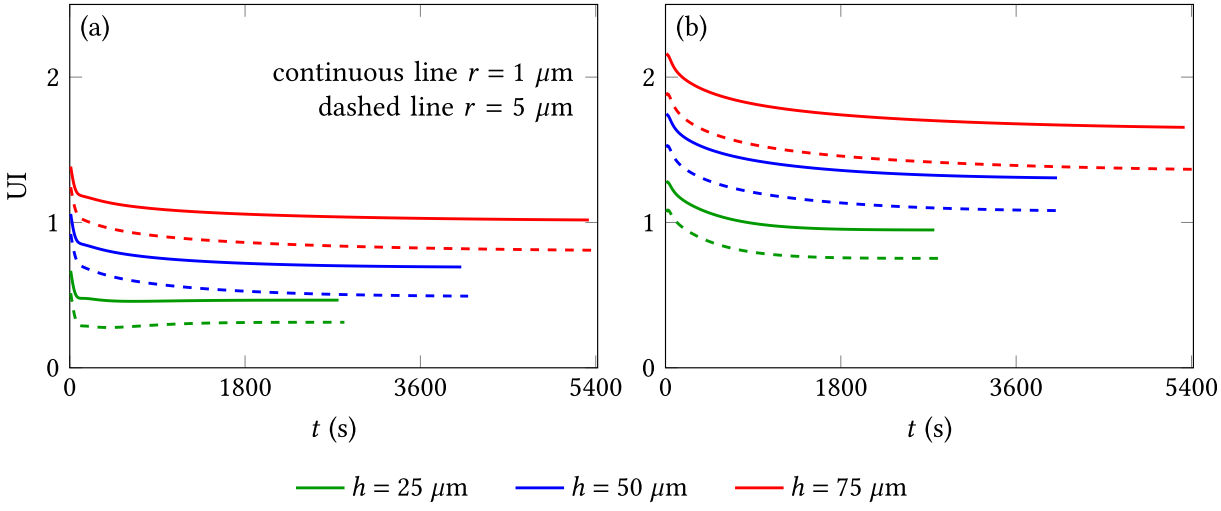

Fig. 4. Time evolution of the uniformity index (25). The performance indicator is evaluated for (a) positive and (b) negative electrode-SPE interfaces. Simulations performed with the purely electrochemical model. A uniform electric current density distribution, corresponding to UI = 0 according to (24) and (25), is approached in batteries with smaller h and larger r. The uniform current distribution is better approached along the $LiCoO_2$/SPE interface (a) than along the C_6/SPE interface (b), irrespective of the cell geometry.

to find the shortest path to the opposing current collector. These observations agree with the numerical results presented in Ref. [18].

Figs. 5 and 6 refer to the $h = 50\ \mu$m cell and focus on the last step of the simulation ($t = 4020$ s for $r = 1\ \mu$m, $t = 4090$ s for $r = 5\ \mu$m); however, the observations that follow are general and apply to any cell geometry and to any simulation time. Fig. 5 shows a contour plot of the electric current density intensity defined as

$$j = \sqrt{j_x^2 + j_y^2}\,. \tag{35}$$

The trenches provide the most conductive path for the charge transfer from one current collector to the other, being the electronic conduction through the electrodes more favorable than the ionic conduction through the SPE. This results in an intense charge flux through the trenches that further increases at their feet. By considering for example the negative electrode, the charges moving from the current collector (bottom) towards the trench tip (top) are collected at the foot of the trench, resulting in a local current density much higher than the average value. A similar process takes place within the positive electrode but with charges moving from the tip toward the foot of the trench. The conversion between electronic and ionic conduction across the negative electrode-SPE interface takes place almost exclusively at the trench tip corner, while it is smoother along the positive electrode-SPE interface. By comparing Fig. 5a and b it is apparent that the charge transfer localization at the corners is strongly reduced in the smoother profile.

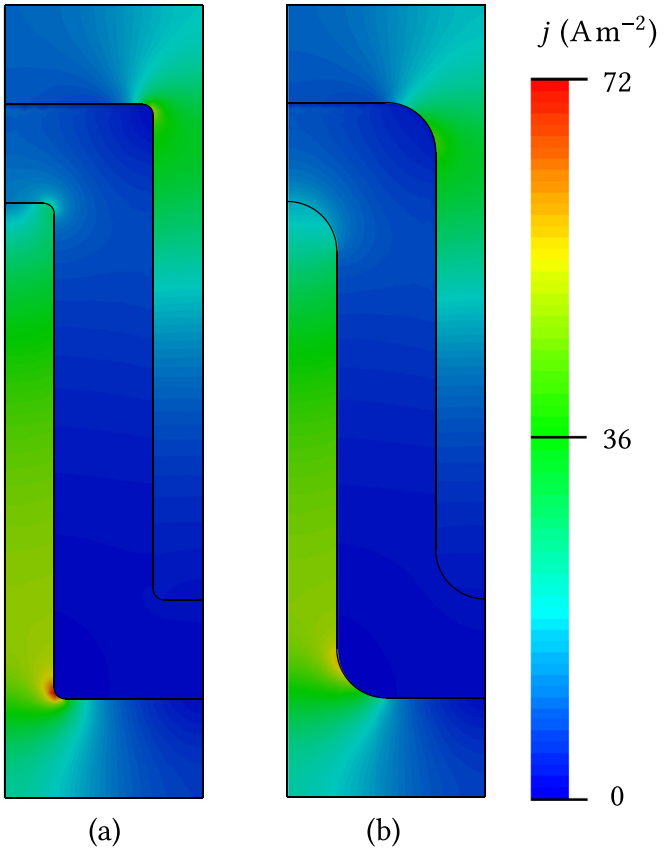

Fig. 5. Electric current density intensity profile (35) in the $h = 50\ \mu$m cell. The plots refer to (a) $r = 1\ \mu$m cell at $t_{end} = 4020$ s and (b) $r = 5\ \mu$m cell at $t_{end} = 4090$ s. Simulations performed with the purely electrochemical model. The trenches provide the most conductive path for the charge transfer from one current collector to the other.

Fig. 6b shows the component of the electric current density (j_{Pos} and j_{Neg} (12)) normal to the electrode-electrolyte interface and the mean electric current ($\bar{j}_{int}$ (22)) evaluated at the same instant of time to which the profiles refer. The mean electric current densities for the $r = 1\ \mu$m and $r = 5\ \mu$m geometries differ to such a small extent that one set of data instead of the average is reported in the plot. The abscissa s represents the coordinate along each interface, Fig. 6a, with $s = 0$ and $s = l$ referring to the points laying on the left- and right-hand sides of the domain, respectively. By comparing the plots against the mean electric current, it appears that the profile referring to the C_6-SPE interface presents spikes which are not visible for the $LiCoO_2$-SPE interface and this leads to a larger value of the uniformity index for the negative electrode (Fig. 4). When plotting j_{el} against s, the current density localizations that appear at the corners (Fig. 5) can be easily recognized. For the $r = 1\ \mu$m cell, the peak observed at $s \approx 5\ \mu$m along the negative electrode-SPE interface corresponds to the electrode trench tip corner, while the sign inversions located at $s \approx 55\ (15)\ \mu$m along the C_6-SPE ($LiCoO_2$-SPE) interface corresponds to the trenches feet.[1] The profiles appear smoothed at both interfaces for the $r = 5\ \mu$m cell, with peak values reduced up to 40%. This was clearly pointed out by the UI reduction attained in geometries with $r = 5\ \mu$m in the plots of Fig. 4, proving that UI is a suitable indicator for the evaluation of the electrode utilization.

4.2. Electrochemical-mechanical model

The effect of electrochemical-mechanical coupling on the ionic conductivity in the SPE is discussed in this section. The numerical simulations are performed by adopting the coupled electrochemical-mechanical formulation described in Section 2.1, without externally applied mechanical solicitations ($\Delta u = 0$). Figs. 7 and 8 refer to the $h = 50\ \mu$m cell. The plots are obtained with combined partial molar volume $\Omega = 1.5 \times 10^{-4}$ m^3 mol^{-1}, simply identified as partial molar volume from now on.

The time evolution of the average electric current densities is reported in Fig. 7a. All curves follow the trend observed in Fig. 3 for the simulations performed with the purely electrochemical model, also reported in the plot and identified by the label ec. Increasingly high values of the Young's modulus lead to narrower variation ranges of the electric current density during the process. The inset in Fig. 7a shows that the initial peak reduces up to 11% (points in the inset are reported starting from $t = 10$ s; being the current equal to zero for $t = 0$, the inclusion of this values makes the graph less readable), while an increase up to 14% is observed for the final value. Due to the stronger inertia of ions to redistribution caused by the electrochemical-mechanical coupling, a shorter interval of time is required in the cells with stiffer polymer to reach the steady state configuration, which is actually achieved for $E = 140$ and 500 MPa.

[1] The reason of the sign inversion is twofold. First, the post-processing procedure with which the electric current density is extrapolated from the integration points to the nodes along the boundary is done from the electrodes side. This choice was made because the definition (1) of the electric current density in the electrodes involves a single variable, ϕ, and thus the post-processing manipulation is easier and less prone to error (averaging between different elements has to be done for only for one degree of freedom). Second, there is a strong localization of the electric current density at the feet of the trenches, where the direction of the normal along the boundary also changes rapidly and becomes opposite to the current density extrapolated to the nodes. If the extrapolation from integration point to interface nodes were done from the SPE elements, the same problem would have appeared in other locations where other variables (either the concentration or the stresses) localize. However, apart from a few specific locations the same plot would have been observed.

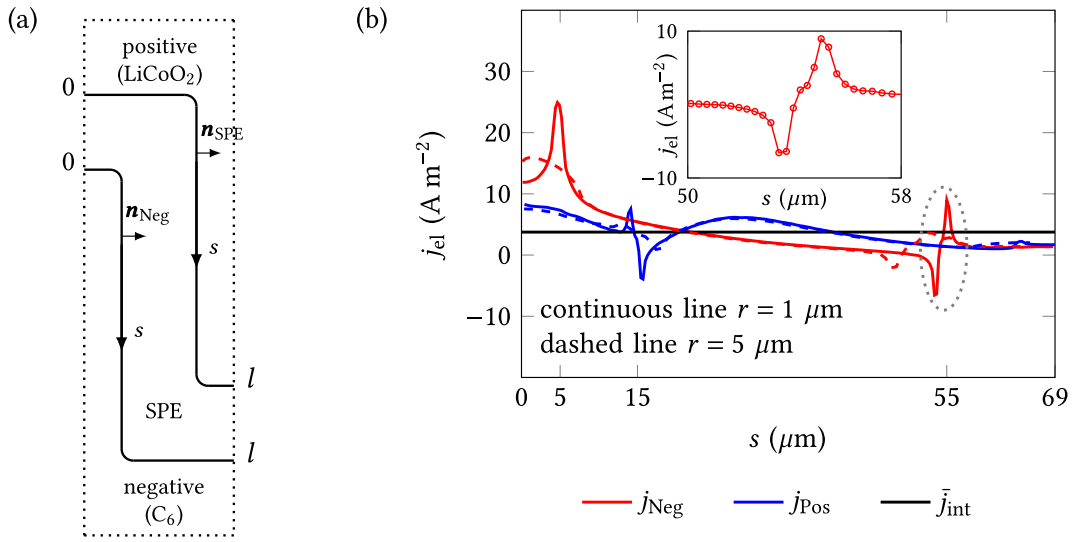

Fig. 6. Distribution of the component of the electric current density normal to the electrode-electrolyte interface along the interface between the electrodes and the SPE (12). (a) Schematic of the domain highlighting conventions for coordinate s and normal $\boldsymbol{n}$. (b) Results referring to the $h = 50$ μm battery ($l \approx 69.0$ μm for $r = 1$ μm, $l \approx 65.5$ μm for $r = 5$ μm): the trend of j_{el} in the proximity of the foot of the negative electrode trench (dotted ellipse for $s \approx 55$ μm) is magnified in the inset and the dots relate to the discretization along the interface. Simulations performed with the purely electrochemical model.

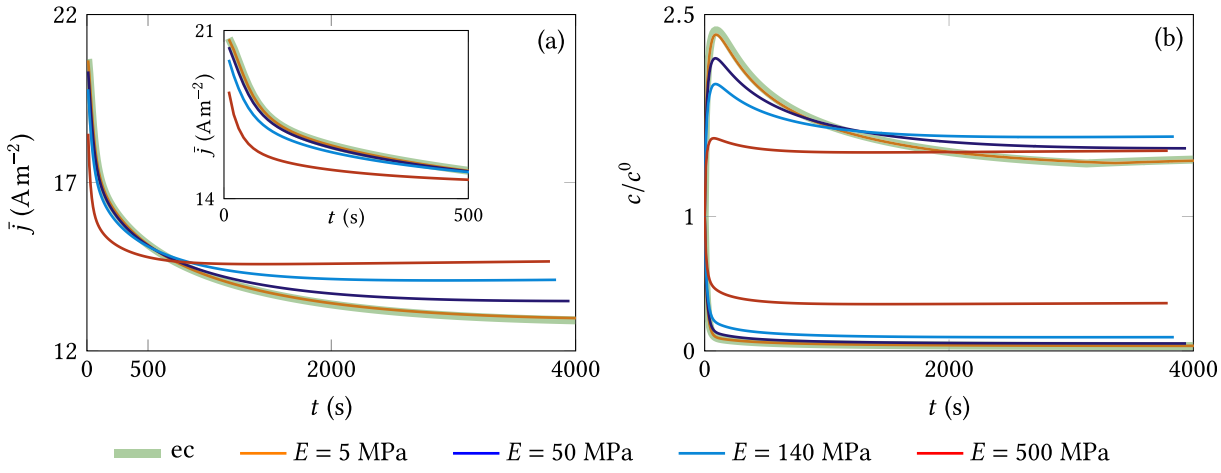

Fig. 7. Time evolution of the (a) electric current density and (b) maximum and minimum ionic concentration in the SPE, for the $h = 50$ μm trench battery with $r = 1$ μm. Simulations performed with $\Omega = 1.5 \times 10^{-4}$ m^3 mol^{-1}. The solution obtained with the purely electrochemical model (ec) is reported for reference. Increasingly high values of the Young's modulus lead to reduced variation ranges of electric current density and ionic concentration.

As for the purely electrochemical model (Fig. 3), cells with $r = 5$ μm are characterized by an electric current density slightly lower than cells with $r = 1$ μm. Data for $r = 5$ μm are not reported in the plot for the sake of readability.

Fig. 7b shows the time evolution of the maximum and minimum values of the ionic concentration attained in the SPE, normalized with respect to the initial concentration c^0 (both normalized values are equal to 1 at $t = 0$, when the concentration distribution is uniform). The higher the elastic modulus of the polymer the higher the pressure induced by ions redistribution, which in turn limits the extent of the ionic concentration gradient. The reduction of the peak value of the maximum concentration is up to 34% while a tenfold increase in the minimum value achieved by ionic concentration is observed for the $E = 500$ MPa polymer with respect to softer polymers. This second observation has a strong impact on possible battery applications, suggesting that the stiffer SPE is less prone to experience a complete depletion of ions even for higher electrostatic potential differences applied between the current collectors. A discussion about the effect of mechanical stresses on the limiting current dictated by the concentration gradient that develops in the SPE is given in a companion paper [25].

Figs. 8a–b show the time evolution of the uniformity index evaluated along the interface between the SPE and each electrode. The range of variation of UI is narrower for stiffer SPEs, indicating that stresses oppose to ionic concentration redistribution also along the electrode-SPE interface. Fig. 8b highlights this aspect and shows that the influence of the stresses is so large for $E = 500$ MPa that UI undergoes an opposite pattern with respect to all the other cases: a minimum value is achieved after a few seconds followed by a monotonic increase toward a plateau. The uniformity index

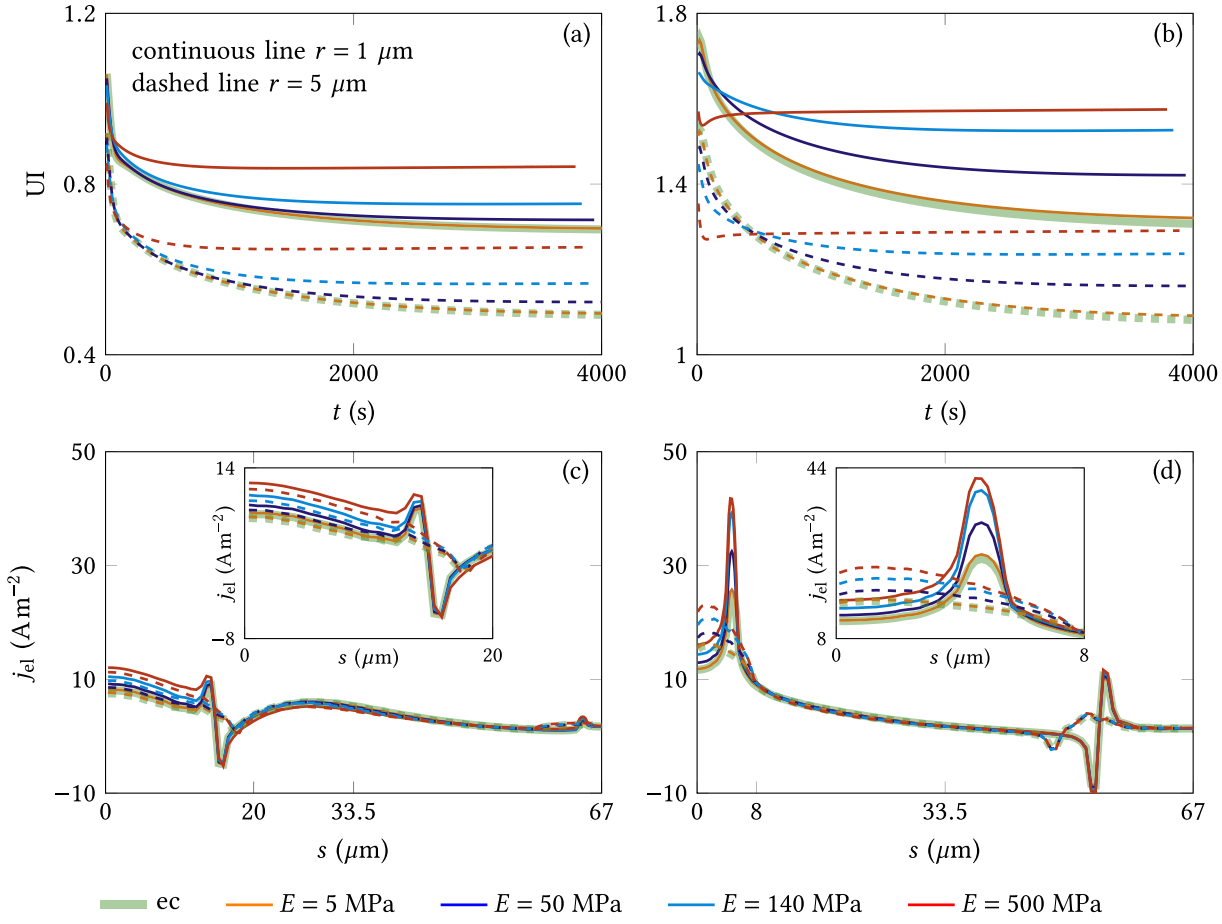

Fig. 8. Time evolution of the uniformity index (25) (a,b), and distribution of the component of the electric current density normal to the electrode-SPE interface along the interface itself (Fig. 6a) (c,d). The plots refer to: (a,c) positive electrode-SPE interface and (b,d) negative electrode-SPE interface. All figures refer to simulations performed on the $h = 50$ μm trench battery using $\Omega = 1.5 \times 10^{-4}$ m^3 mol^{-1}. The solution obtained with the purely electrochemical model (ec) is reported for reference. The trend of j_{el} at the foot of the positive electrode and at the tip of the negative electrode is magnified in (c) and (d), respectively. Increasingly high values of the Young's modulus lead to current density profiles that progressively diverge from the uniform distribution (higher UI).

increases (between 20 and 30% with respect to the purely electrochemical model, depending on the trench tip radius) for increasingly high values of the Young's modulus, i.e., the utilization of the electrode is restricted to narrower regions when higher values of stresses develop due to ionic redistribution in the SPE. This can be better understood from Figs. 8c–d in which the distribution of the component of the electric current density normal to the electrode-SPE interface along the interface is reported. Modifications of the electric current density profile are appreciable only in the region between the bottom part of the positive electrode ($s \in [0, 20\ \mu\text{m}]$, Fig. 8c) and the tip of the negative electrode ($s \in [0, 8\ \mu\text{m}]$, Fig. 8d). The peak value reached along the negative electrode-SPE interface increases up to 68% (45%) moving from $E = 0$ to 500 MPa for $R = 1(5)$ μm indicating that the negative trench tip is the most sensitive location for the overall battery performance. For the positive electrode-SPE interface the variation at the bottom part are up to 48%. The favorable effect of smooth geometries on the homogeneous utilization of the electrode is visible also when the stress contribution is considered: larger corner radii lead to reduced UI values.

Ionic concentration and stresses distribution within the SPE are examined for the 50 μm trench batteries and $E = 140$ MPa, with results reported in Figs. 9–11. Fig. 9 shows the concentration distribution when the maximum ionic concentration peak is achieved (Fig. 7b) and at t_{end}. The ionic concentration gradient is more pronounced at the tip of the negative electrode trench than elsewhere, irrespective of the battery geometry and the state of progress of the discharge process. This clarifies why the effects of electrochemical-mechanical coupling on the electric current density observed in Figs. 8c–d is limited to that region: the impact of stresses on the ionic conduction is directly proportional to the magnitude of the ionic concentration gradient. Analogous comments apply to concentration distributions determined for different trench heights although local values are different in agreement with Ref. [18].

Figs. 10 and 11 refer to the $h = 50$ μm cell with $r = 1$ and 5 μm. They show the distribution of pressure (p) and von Mises stress (σ_{vM}) corresponding to the ionic distributions of Fig. 9. A compressive stress state initially arises at the tip of the negative electrode trench when the ionic concentration is maximum at that location (Figs. 10a–b and 9a-b). The concentration redistributes afterwards and the pressure relaxes as shown in Figs. 9c–d and 10c-d, but the depletion of the region at the bottom of the positive electrode trench causes a tensile stress to develop.

The entity of the tractions is remarkably high if one considers on the one hand that these values correspond to the threshold for

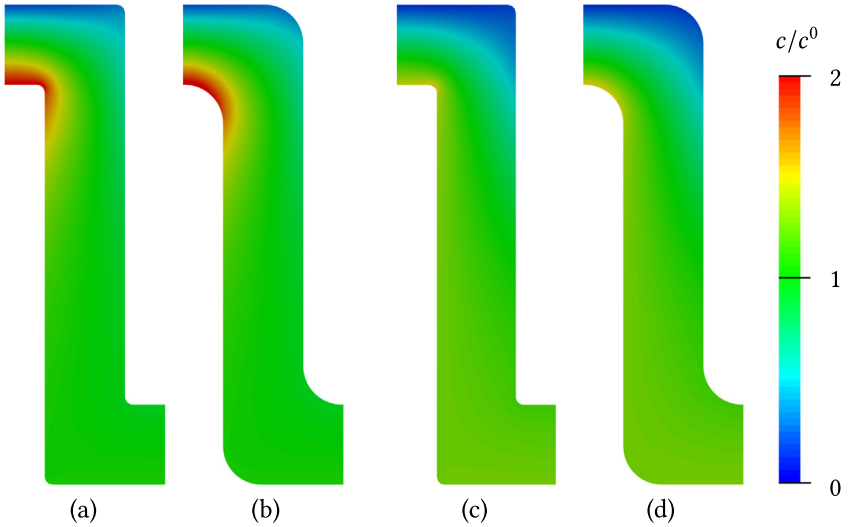

Fig. 9. Contour plots of the ionic concentration distribution within the SPE for the $h = 50$ μm cell and tip corners radii (a,c) $r = 1$ μm and (b,d) $r = 5$ μm. Simulations performed with and $E = 140$ MPa. The plots refer to (a,b) the instant of time at which the maximum concentration value is achieved in the cell (Fig. 7b), and (c,d) at time $t = t_{end}$: (a) $t = 80$ s, (b) $t = 70$ s, (c) $t = 3840$ s, (d) $t = 3930$ s. The ionic concentration gradient is more pronounced at the tip of the negative electrode trench than elsewhere, irrespective of the state of progress of the discharge process.

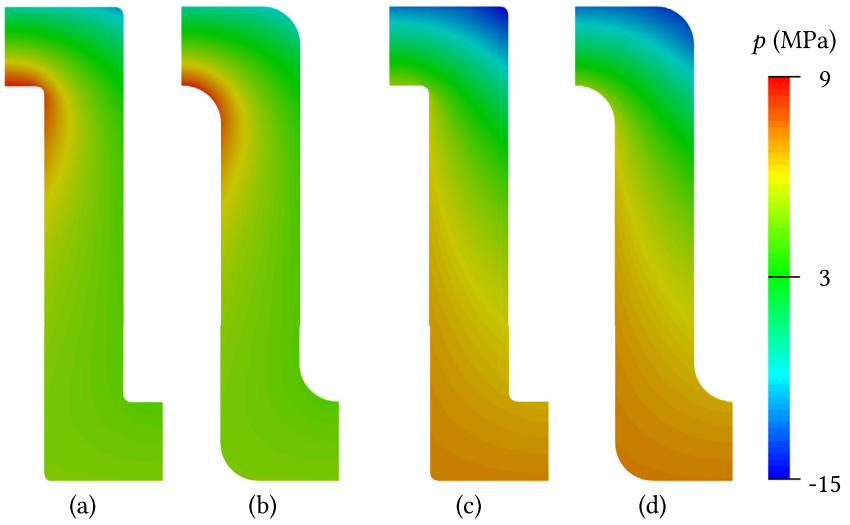

Fig. 10. Contour plots of the pressure distribution within the SPE for the $h = 50$ μm cell and tip corners radii (a,c) $r = 1$ μm and (b,d) $r = 5$ μm. Simulations performed with $\Omega = 1.5 \times 10^{-4}$ m^3 mol^{-1} and $E = 140$ MPa. The plots refer to (a,b) the instant of time at which the maximum concentration value is achieved in the cell (Fig. 7b), and (c,d) at time $t = t_{end}$: (a) $t = 80$ s, (b) $t = 70$ s, (c) $t = 3840$ s, (d) $t = 3930$ s.

fracture stress indicated by experiments [37] for crosslinked PPGDA polymers (about 7% of the Young's modulus), and on the other hand that such a stress field only arises because of regular battery operations, as no external loads are applied. It should be noted that the average electric current density is up to $\bar{j} \approx 20$ A m^{-2} as shown in Figs. 3 and 7a. These loading conditions are much more severe than those considered by Su et al. [10] who performed their experiments with $\bar{j} \approx 2 \times 10^{-3}$ A m^{-2} (an electric current of 1 μA was applied on a 1 inch diameter circular cell) on a uniform planar cell with a SPE thickness $w = 220$ μm. The authors commented that "debonding does not occur during the gentle cycling conditions that were employed, in spite of the low adhesion energy", suggesting that electrode-SPE debonding should be expected under more severe loading conditions, in line with our observations. If detachment of the SPE from the bottom of the positive electrode occurs, the functioning of the battery would be irreversibly compromised as that location lies along the most conductive path of the cell.

The combination of cell geometry and boundary conditions (30–32) causes deviatoric stress components to arise in response of the ionic concentration redistribution. Fig. 11 shows that these deviatoric components lead to a non-zero von Mises stress in the proximity of the negative electrode trench tip, where the highest concentration gradient is located. The von Mises stress distribution within the SPE is basically constant during the entire discharge process (Figs. 11a–b and Figs. 11c–d show no appreciable

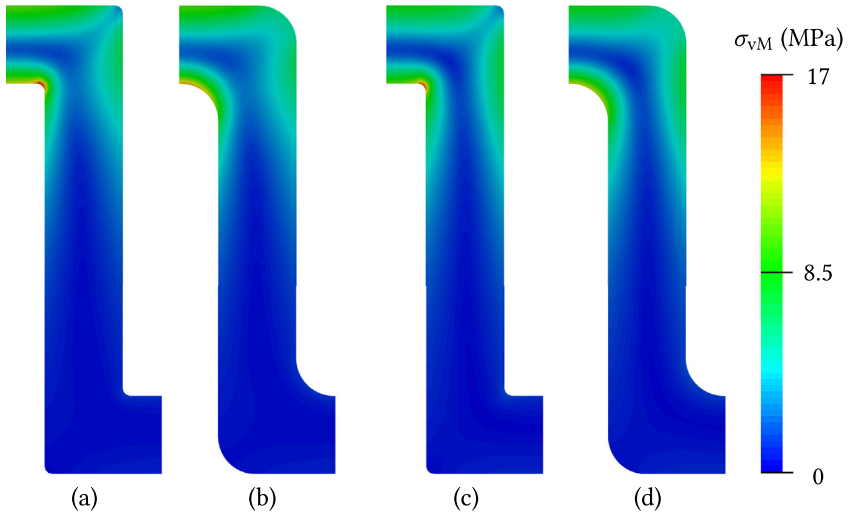

Fig. 11. Contour plots of the von Mises stress distribution within the SPE for the $h = 50\ \mu$m cell and tip corners radii (a,c) $r = 1\ \mu$m and (b,d) $r = 5\ \mu$m. Simulations performed with $\Omega = 1.5 \times 10^{-4}$ m^3 mol^{-1} and $E = 140$ MPa. The plots refer to (a,b) the instant of time at which the maximum concentration value is achieved in the cell (Fig. 7b), and (c,d) at time $t = t_{end}$: (a) $t = 80$ s, (b) $t = 70$ s, (c) $t = 3840$ s, (d) $t = 3930$ s. The von Mises stress attains its maximum value at the negative electrode trench tip.

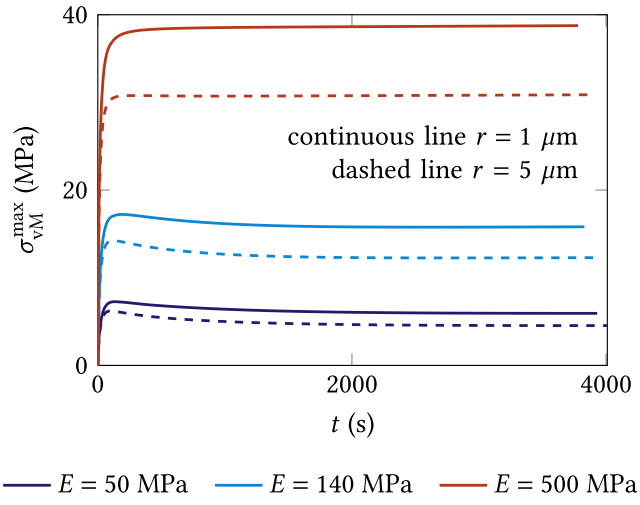

Fig. 12. Time evolution of the maximum von Mises stress achieved within the SPE, for the $h = 50\ \mu$m cell, simulations performed with $\Omega = 1.5 \times 10^{-4}$ m^3 mol^{-1}. The maximum von Mises stress becomes constant after a short transient (compare with Fig. 11).

differences). This observation is strengthen by Fig. 12 in which the time evolution of the maximum value achieved by the von Mises stress within the SPE is reported for $h = 50\ \mu$m and $\Omega = 1.5 \times 10^{-4}$ m^{3}mol^{-1} and for both $r = 1$ and 5 μm (data for $E = 5$ MPa are not included in the graph because the corresponding von Mises stress is 0.8 MPa at the most). Plots analogous to those shown in Fig. 12 but for cells with different trench heights and $\Omega = 1.1 \times 10^{-4}$ m^{3}mol^{-1} are not reported because of their resemblance in terms of trend and numerical values. This suggests that the parameter with the biggest impact on the maximum von Mises stress is the corner radius of the electrode trenches.

Experimental studies on PEO with Young's modulus in the range 2–50 MPa and 70–325 MPa were performed by Westover et al. [34] and Moreno et al. [36], respectively. These studies show that either the yield stress [34] or tensile strength [36] of this material falls in the range 3–10% of the Young's modulus of the polymer. In this perspective, the linear elastic constitutive model here adopted appears to provide a reasonable first approximation of the observed behavior. By taking a yield stress $\sigma_Y \approx 0.1\ E$, Fig. 11 shows that the von Mises stress exceeds this value only in a confined region. It must be noted however that the location where the maximum von Mises stress is achieved is extremely relevant for the overall battery performance, as it corresponds to the corner tip of the negative electrode where most of the electric current transfer between electrode and SPE occurs (Fig. 6b). Irreversible deformations or damage of the SPE at this location can potentially lead to modifications of the electrochemical properties of the polymer electrolyte that would in turn affect the cell conduction path and its overall conductivity—analysis of the implication of mechanical damage in solid inorganic electrolyte on the battery performance can be found in Refs. [50,51]. Even with no external loads applied to the cell, the simulations show that the yield stress in the SPE can be reached during routine battery operations. In the first instance, the model at hand can provide insight into a battery design that ensures structural integrity of the solid electrolyte. By simply changing the corner radius from 1 to 5 μm, for example, the maximum von Mises stress reduces from 17 MPa to 14 MPa thus limiting the above mentioned risks.

To summarize the results obtained for different cell geometries, Fig. 13 shows a few selected quantities for the examined values of the Young's modulus and for $\Omega = 1.1 \times 10^{-4}$ m^{3}mol^{-1} (a,c,e) and $\Omega = 1.5 \times 10^{-4}$ m^{3}mol^{-1} (b,d,f). The results are normalized by corresponding data obtained with the purely electrochemical model identified by the subscript ec. Figs. 13a–b show the cell conductivity (14) evaluated using the electric current density at t_{end}, here simply called, with abuse of terminology, “steady state conductivity”. The plots show that the enhancement of conductivity is directly proportional to the Young's modulus. The only exception is represented by the $h = 25\ \mu$m cell with $r = 5\ \mu$m and $\Omega = 1.5 \times 10^{-4}$ m^{3}mol^{-1}, for which a reduced conductivity is observed from $E = 140$ to $E = 500$ MPa (Fig. 13b). This suggests that the beneficial effects of electrochemical-mechanical coupling reaches a maximum for $E \approx 140$ MPa, and beyond this value the

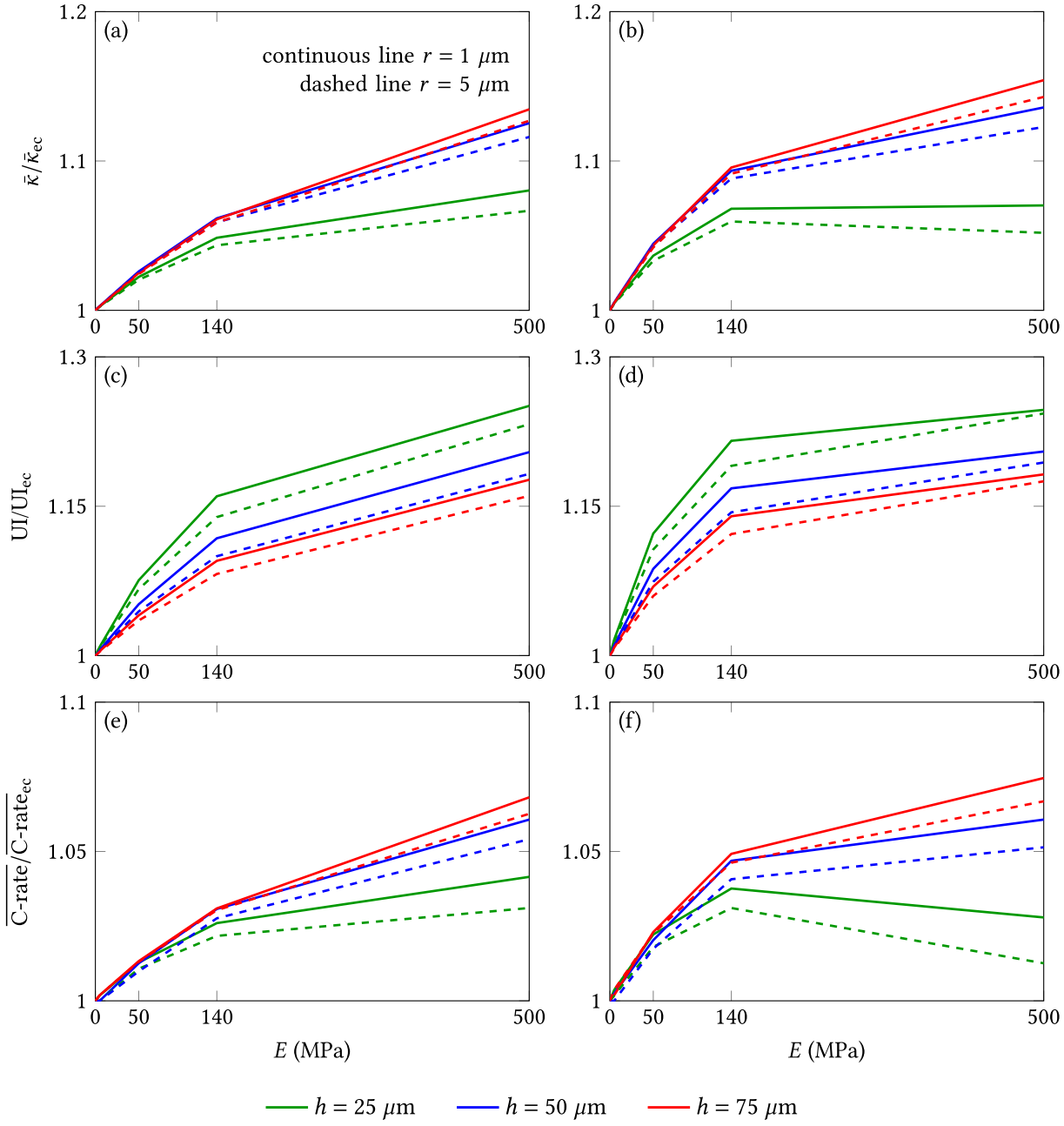

Fig. 13. Cell performance versus Young's modulus of the SPE: (a,b) system conductivity (14) evaluated at $t = t_{end}$; (c,d) uniformity index (25) evaluated along the negative electrode interface at $t = t_{end}$; (e,f) $\overline{\text{C-rate}}$ (36). Plots in (a,c,e) and (b,d,f) refer to $\Omega = 1.1 \times 10^{-4}$ and 1.5×10^{-4} μm, respectively. Plots scaled by a reference value obtained from a simulation on the same battery geometry with the purely electrochemical model. The beneficial effect of the electrochemical-mechanical coupling is more pronounced in batteries with higher trenches: larger increase of $\bar{\kappa}$ and $\overline{\text{C-rate}}$ and reduced increase of UI compared to batteries with shorter trenches.

stresses alter the ionic conduction path in a way that is not favorable to ionic conduction. The behavior seems to be related to the specific geometry of the battery and was not observed for the other configurations. The plots reveal that the favorable effects of electrochemical-mechanical coupling on the system conductivity is more pronounced for cells with longer trenches, up to a maximum enhancement of 15%. A pronounced gap separates the $h = 25$ μm cell from the others, suggesting that there exists a threshold in trench height after which the effects of electrochemical-mechanical coupling on the overall behavior becomes stable.

Figs. 13c–d report the trend of the uniformity index (25) relative to the negative electrode evaluated at t_{end} versus the Young's modulus of the SPE. Changes in the electrode utilization with E follow the opposite trend with respect to the system conductivity: the entity of UI variations with the Young's modulus of the SPE is inversely proportional to the trench height, up to 25% for the $h = 25$ μm cell. This holds true for all battery geometries and for both values of the partial molar volume.

A measure of the impact of E on the entire discharge process is provided by the average C-rate defined as

$$\overline{\text{C-rate}} = \frac{1\ \text{hour}}{t_{\text{end}}}\ . \tag{36}$$

Since the cell discharges under potentiostatic conditions, the potential difference between the current collectors is assigned and constant, ΔV_{disc}, and $\overline{\kappa}$ is proportional to the electric current density flowing through the cell at any instant of time. The quantity defined by (36) indirectly expresses the average behavior of the cell conductivity over time, with

$$\overline{S}\,|\Delta V_{\text{disc}}| \int_0^{t_{\text{end}}} \overline{\kappa}\,\mathrm{d}t \;=\; C_{\text{cell}} \tag{37}$$

following from (14). Higher $\overline{\text{C-rate}}$ values correspond to higher average cell conductivities.

Figs. 13e–f show that the trend of $\overline{\text{C-rate}}$ versus E is similar to that of $\overline{\kappa}$ versus E (Figs. 13a–b): the beneficial effect of the electrochemical-mechanical coupling is more pronounced in batteries with higher trenches ($\overline{\text{C-rate}}$ shows an increase up to 7% in the $h = 75\ \mu$m cell). The $\overline{\text{C-rate}}$ enhancement is less pronounced than that of steady state system conductivity because it also accounts for the initial transient behavior. As shown in Fig. 7a, the presence of stresses leads to an increased inertia to ionic concentration redistribution, making the SPE less conductive during the initial part of the discharge process (a few hundred seconds). The importance of the initial ionic conduction reduction is major for the 25 μm high trench cell, for which the transient stage constitutes a larger portion of the entire discharge process. This causes the reduction of $\overline{\text{C-rate}}$ observed in Fig. 13f from $E = 140$ MPa to $E = 500$ MPa.

According to these results, SPEs characterized by higher elastic moduli are more suitable for cells with longer trenches, as the beneficial effects of electrochemical-mechanical coupling on both the maximum achievable current density (system conductivity) and the average C-rate is more pronounced, while the unfavorable effect of stresses on electrode utilization is more moderate with respect to shorter trench batteries.

4.3. Electrochemical-mechanical model with external loads

The effect of externally applied loads on the battery performance is investigated by means of numerical simulations with different values of the displacement boundary condition Δu: 0, 0.25, 0.5 and 1 μm. The pressure levels proportional to those displacements are in the ranges: 0.2–0.8 MPa for $E = 5$ MPa; 2–8 MPa for $E = 50$ MPa; 5–23 MPa for $E = 140$ MPa; and 19–78 MPa for $E = 500$ MPa. The pressure values are higher than those considered in previous experimental studies aiming at reproducing cell pressure states induced during manufacturing, in which external pressures up to 2 MPa and 5 MPa were applied on single cells [52] and pouch cells [53], respectively. However, the average compressive stress experienced by particle-based electrode has proved to exceed that applied during manufacturing process (Sethuramn et al. [54] report values up to 13 MPa). The largest values of pressure, corresponding to the boundary condition $\Delta u = 1\ \mu$m, are assumed to be induced by external solicitations applied on the cell during service. Boundary condition $\Delta u = 1\ \mu$m should be regarded as the upper bound for the validity of the infinitesimal strain theory, since it induces a 10% vertical deformation.

Pressure and von Mises stress distributions in Fig. 14 for $\Delta u = 0.5\ \mu$m are contrasted to those related to the same cell geometries and material parameters when no external loads are applied (Figs. 10c–d and 11c-d). As expected, the applied displacement induces a compressive stress state at both trench tips that increases the compressive stress at the bottom and lowers the tractions at the top of the region occupied by the SPE. The von Mises stresses, previously confined around the positive electrode trench tip (Fig. 11) is non-zero in the entire cell. In this new configuration, the von Mises stress approaches 15 MPa (above 0.1 E) at the bottom part of the positive electrode (the location that faces the middle point of the negative trench tip) for both values of r. A peak value is achieved at the positive trench tip for $r = 1\ \mu$m, suggesting that, depending on the configuration of the external loads, different locations in the SPE may undergo irreversible deformations. It should be noted that, according to the stress maps provided in Fig. 14, the $r = 5\ \mu$m geometry proves to be a better option toward the reduction of stress concentration and the risk of battery failure.

The effect of external loads on the $h = 50\ \mu$m cell with different values of Young's modulus and partial molar volume is summarized in Fig. 15. All the reported quantities show a linear dependence on Δu for any considered value of the SPE Young's modulus.

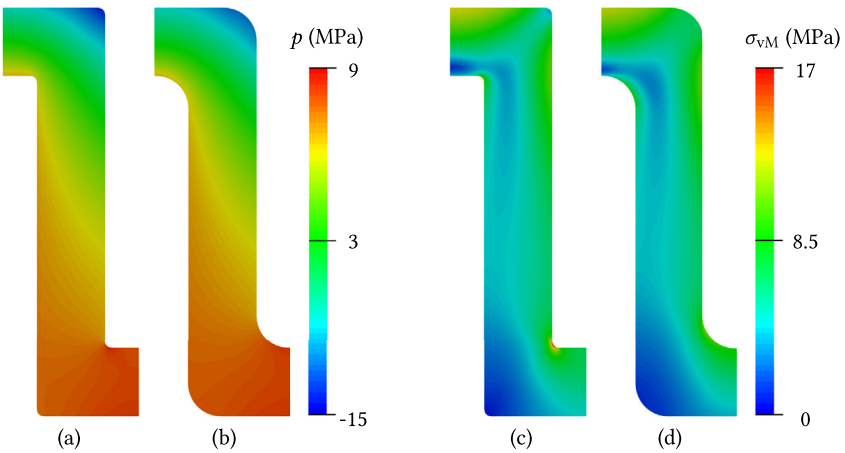

Fig. 14. Contour plots of the pressure (a,b) and the von Mises stress (c,d) distribution within the SPE for the $h = 50\ \mu$m cell and tip corners radii (a,c) $r = 1\ \mu$m and (b,d) $r = 5\ \mu$m. Simulations performed with $\Omega = 1.5 \times 10^{-4}$ m^3 mol^{-1}, $E = 140$ MPa and $\Delta u = 0.5\ \mu$m. The plots refer to time $t = t_{\text{end}}$: (a,c) $t = 3930$ s, (b,d) $t = 4000$ s.

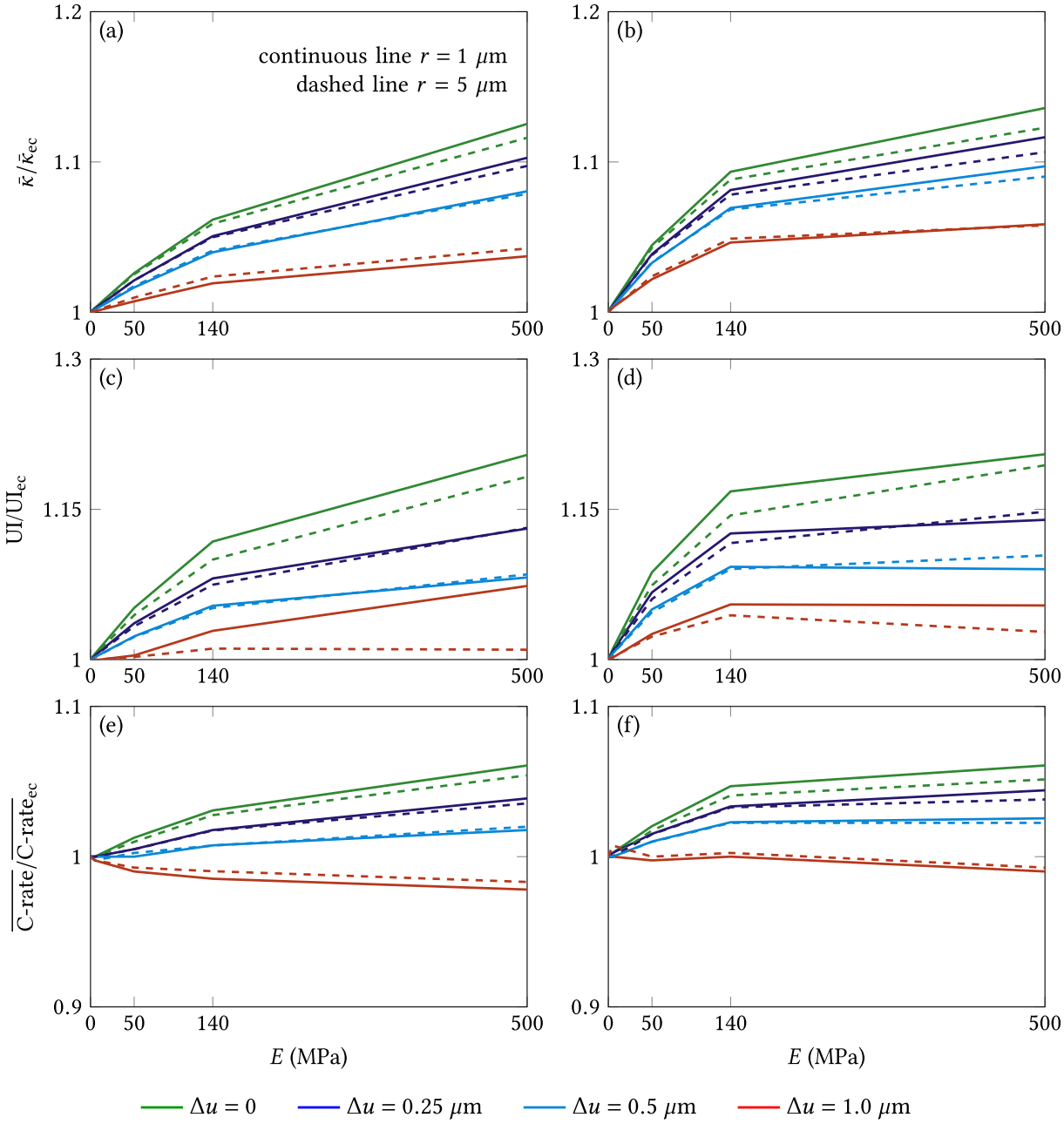

Fig. 15. Cell performance versus Young's modulus of the SPE: (a,b) system conductivity (14) evaluated at $t = t_{end}$; (c,d) uniformity index (25) evaluated along the negative electrode interface at $t = t_{end}$; (e,f) average C-rate (36). Plots in (a,c,e) and (b,d,f) refer to $\Omega = 1.1 \times 10^{-4}$ and 1.5×10^{-4} μm respectively. Pots scaled by a reference value obtained from a simulation on the same battery geometry with the purely electrochemical model. The contribution of the stresses on the cell performance is beneficial even if deformations on the SPE are externally induced, provided that Δu is only slightly above 5 μm. Figs. 15e–f show that a reduction of $\overline{\text{C-rate}}$ compared to the purely electrochemical solution is observed only for $\Delta u = 1$ μm.

Figs. 15a–b and Figs. 15e–f reflect the progressive reduction of the steady state and the average (throughout the overall process) current densities, respectively, for increasingly high values of the applied displacement. Increasingly high values of the external displacement cause a reduction of the cell current, more than 5% by changing Δu from 0 to 1 μm, represented by a progressive shift of the curves downward. A similar experimental evidence was reported by Mussa et al. [52] who observed an overall impedance increase in fresh cells (before any aging took place, which is the case here because no such mechanisms are considered in the analyses) subjected to increasingly high values of external pressure. The contribution of the stresses on the cell performance is beneficial also when deformations on the SPE are externally induced, provided that the amplitude of the applied displacement is below a certain threshold, identified as Δu slightly above 5 μm for the systems considered in this study (Figs. 15e–f). The average electric current is lower than the reference value only for $\Delta u = 1$ μm, irrespective of the value of E. This is in agreement with experimental studies conducted on porous electrode showing that the application of an external pressure to the cell leads to improved

performance, provided that the extent of the applied pressure is limited [52,53]. Figs. 15c–d show that the uniformity index generally decreases for larger Δu. The lower values of UI do not follow from a favorable redistribution of the exchange current density toward a uniform utilization of the electrodes: they are related to the reduction of the electric current density in the region of the cell above the negative electrode trench tip. The latter are due to a reduced ionic conductivity caused by the presence of an externally induced compressive stress field in the SPE that alters the ionic conduction path.

5. Conclusions

Discharge processes in microbatteries with a trench geometry are simulated using a coupled electrochemical-mechanical model. Due to the complex geometry of the battery, the overall conduction path (from one current collector to the other) determines the distribution of ions in the SPE. The stress field in the SPE follows from a non-uniform concentration profile, so that the mechanical response of the polymer cannot be predicted without the inclusion of all the battery components in the analyses.

A cell conduction enhancement is predicted when the coupled model is used in place of the purely electrochemical model. In general, the pressure arising in the SPE layer limits the development of non-uniform concentration profiles, enhancing the ionic transport. This study proves that the role of mechanical stresses cannot be neglected and should be accounted for in battery design [26] and geometry optimization [20] because the pressure (due to either ionic redistribution or externally applied solicitation) locally affects the electric current density. Previous experimental studies have shown that non-uniform current density distributions favor side reactions that reduce cyclable lithium [53] and accelerate non-uniform aging [52] resulting in capacity fade. Even if the incorporation of the reaction kinetic and the electrodes expansion/contraction in the model would lead to more complex responses, dictated by the dynamic behavior of each cell component, the general trend of the role of mechanical stresses is expected to be similar to that observed in this study. Our results indicates that the electrode-SPE interface is the most delicate location in terms of mechanical integrity, in agreement with recent numerical [24] and experimental [10,26] studies, as both pressure and von Mises stress values attain their maximum values therein.

It is known that the mechanical response of the SPE depends on the time scales at which the solicitations occur. The combined experimental and numerical study by Su et al. [10] shows that the strain rate experienced by a SPE placed in a working battery may strongly differ from the strain rates at which the material is tested when its mechanical properties are determined. The strain rate induced by the ionic redistribution occurring in the SPE was up to 4×10^{-3} s^{-1} in our simulations. Experimental evidence [35,36,55] however indicates a rate-dependent behavior in mechanical tests conducted at comparable strain rate levels. This suggests that a model accounting for the SPE viscous response would provide a more realistic prediction of the electrochemical-mechanical behavior. However, by comparing the stress values resulting from our simulations with those indicated as limit values of the elastic regime in PEO and PPGDA [34,36,37], the linear elastic constitutive model used for the polymer electrolyte can be considered as an acceptable approximation in this study.

Conflicts of interest

There are no conflicts to declare.

Acknowledgements

The research leading to these results has received funding from the European Research Council under the European Union's Seventh Framework Programme (FP7/2007–2013)/ERC Grant agreement no 617972.

Appendix A. Numerical implementation

The governing equations in Section 2.1 define an initial boundary value problem. The charge conservation equations for the electrodes (2) and the coupled system of equations for the SPE (9) must be solved simultaneously. The problem can be formulated in a weak form by multiplying the strong form (governing equations (2)–(9)) by a suitable set of test functions and performing an integration by parts over the domain. Adopting a Galerkin approach, the weak form is built using variations of the same variables that rule the problem, namely electrostatic potential $\widehat{\phi}$, concentration $\widehat{c}$, displacements $\widehat{\boldsymbol{u}}$ and pressure $\widehat{p}$:

$$\kappa_{\mathrm{Pos}} \int_{V_{\mathrm{Pos}}} \nabla\widehat{\phi}\cdot\nabla\phi \,\mathrm{d}V + \int_{\partial V_{\mathrm{Pos}}\cap\partial V_{\mathrm{cc}}} \widehat{\phi}\, j_{\mathrm{Pos\ cc}} \,\mathrm{d}V - \int_{\partial V_{\mathrm{SPE}}\cap\partial V_{\mathrm{Pos}}} \widehat{\phi}\, j_{\mathrm{Pos}} \,\mathrm{d}V = 0, \tag{A.1a}$$

$$\kappa_{\mathrm{Neg}} \int_{V_{\mathrm{Neg}}} \nabla\widehat{\phi}\cdot\nabla\phi \,\mathrm{d}V + \int_{\partial V_{\mathrm{Neg}}\cap\partial V_{\mathrm{cc}}} \widehat{\phi}\, j_{\mathrm{Neg\ cc}} \,\mathrm{d}V + \int_{\partial V_{\mathrm{SPE}}\cap\partial V_{\mathrm{Neg}}} \widehat{\phi}\, j_{\mathrm{Neg}} \,\mathrm{d}V = 0, \tag{A.1b}$$

$$\gamma_\phi \int_{V_{\mathrm{SPE}}} \nabla\widehat{\phi}\cdot c\,\nabla\phi \,\mathrm{d}V - \gamma_c \int_{V_{\mathrm{SPE}}} \nabla\widehat{\phi}\cdot\nabla c \,\mathrm{d}V - \gamma_p \int_{V_{\mathrm{SPE}}} \nabla\widehat{\phi}\cdot c\,\nabla p \,\mathrm{d}V + \int_{\partial V_{\mathrm{SPE}}\cap\partial V_{\mathrm{Pos}}} \widehat{\phi}\, j_{\mathrm{Pos}} \,\mathrm{d}V - \int_{\partial V_{\mathrm{SPE}}\cap\partial V_{\mathrm{Neg}}} \widehat{\phi}\, j_{\mathrm{Neg}} \,\mathrm{d}V = 0, \tag{A.1c}$$

$$\int_{V_{\mathrm{SPE}}} \widehat{c}\,\frac{\partial c}{\partial t} \,\mathrm{d}V + D\int_{V_{\mathrm{SPE}}} \nabla\widehat{c}\cdot\nabla c \,\mathrm{d}V + \frac{1}{2}\frac{D}{RT}\Omega\int_{V_{\mathrm{SPE}}} \nabla c\cdot c\,\nabla p \,\mathrm{d}V + \frac{1}{F}\frac{D_{\mathrm{X}^-}}{D_{\mathrm{Li}^+}+D_{\mathrm{X}^-}} \int_{\partial V_{\mathrm{SPE}}\cap\partial V_{\mathrm{Pos}}} \widehat{c}\, j_{\mathrm{Pos}} \,\mathrm{d}V - \frac{1}{F}\frac{D_{\mathrm{X}^-}}{D_{\mathrm{Li}^+}+D_{\mathrm{X}^-}} \int_{\partial V_{\mathrm{SPE}}\cap\partial V_{\mathrm{Neg}}} \widehat{c}\, j_{\mathrm{Neg}} \,\mathrm{d}V = 0, \tag{A.1d}$$

$$\int_{V_{\mathrm{SPE}}} \widehat{\boldsymbol{\varepsilon}} : \mathbf{D}\,\boldsymbol{\varepsilon} \,\mathrm{d}V - K\Omega\int_{V_{\mathrm{SPE}}} \mathrm{tr}\,\widehat{\boldsymbol{\varepsilon}}\,\left(c-c^0\right) \mathrm{d}V - \int_{V_{\mathrm{SPE}}} \widehat{\boldsymbol{u}}\cdot\boldsymbol{t} \,\mathrm{d}V = 0, \tag{A.1e}$$

$$\int_{V_{\mathrm{SPE}}} \widehat{p}\, p \,\mathrm{d}V + K\int_{V_{\mathrm{SPE}}} \widehat{p}\,\mathrm{tr}\,\widehat{\boldsymbol{\varepsilon}} \,\mathrm{d}V - K\Omega\int_{V_{\mathrm{SPE}}} \widehat{p}\,\left(c-c^0\right) \mathrm{d}V = 0\,. \tag{A.1f}$$

Green's formula is used to reduce the order of differentiation. Terms $j_{\mathrm{Pos\ cc}} = \boldsymbol{j}_{\mathrm{Pos}}\cdot\boldsymbol{n}_{\mathrm{Pos}}$, $j_{\mathrm{Neg\ cc}} = \boldsymbol{j}_{\mathrm{Neg}}\cdot\boldsymbol{n}_{\mathrm{Neg}}$ and $\boldsymbol{t}$ are boundary conditions representing the electric current density applied on the boundary of the electrodes and the tractions applied along the boundary of the SPE, respectively. The weak form (A.1) already accounts for the interface conditions (12) and (13). The presence of stress gradients in the governing equations of charge (A.1c) and mass (A.1d) conservation requires the introduction of the pressure (A.1f) as additional degree of freedom [56].

Due to the multiphysics nature of the problem, the field

variables have different units and their values span over ranges that differ by decades. Convergence issues following from an ill-conditioned tangent matrix can be avoided by recasting the weak form (A.1) into its corresponding dimensionless version [27,28]. First, the field variables are a dimensionalized by introducing the scaling factors

$$\phi^* = \frac{F}{RT}\phi, \quad c^* = \frac{1}{c_{\text{ref}}}c, \quad \boldsymbol{u}^* = \frac{1}{l_{\text{ref}}}\boldsymbol{u}, \quad p^* = \frac{\Omega}{RT}p\,. \tag{A.2}$$

Second, each equation of the weak form (A.1) is divided by a factor that makes it dimensionless. We have used

$$(D_{\text{Li}^+} + D_{\text{X}^-})\, RT\, c_{\text{ref}}\, l_{\text{ref}}, \quad \frac{c_{\text{ref}}^2\, l_{\text{ref}}^3}{\Delta t}, \quad K\, l_{\text{ref}}^3, \quad \left(\frac{RT}{\Omega}\right)^2 l_{\text{ref}}^3, \tag{A.3}$$

where the first coefficient refers to (A.1a), (A.1b) and (A.1c), the second to (A.1d), the third to (A.1e) and the last one to (A.1f). The term Δt (expressed in seconds) represents the time step size $\Delta t = t_{n+1} - t_n$ used in the simulations. Terms c_{ref} and l_{ref} represent a reference concentration (here c^0) and a characteristic length of the problem, respectively.

The weak form (A.1) can be rephrased in terms of the non-dimensional quantities ϕ^*, c^*, $\boldsymbol{u}^*$ and p^* as

$$\begin{aligned}
&\frac{RT\,\kappa_{\text{Pos}}}{(D_{\text{Li}^+} + D_{\text{X}^-})\, F^2\, c_{\text{ref}}\, l_{\text{ref}}} \int_{V_{\text{Pos}}} \nabla\widehat{\phi}^* \cdot \nabla\phi^*\, \mathrm{d}V \\
&\quad + \frac{1}{(D_{\text{Li}^+} + D_{\text{X}^-})\, F\, c_{\text{ref}}\, l_{\text{ref}}} \int_{\partial V_{\text{Pos}} \cap \partial V_{\text{cc}}} \widehat{\phi}^*\, j_{\text{Pos cc}}\, \mathrm{d}V \\
&\quad - \frac{1}{(D_{\text{Li}^+} + D_{\text{X}^-})\, F\, c_{\text{ref}}\, l_{\text{ref}}} \int_{\partial V_{\text{SPE}} \cap \partial V_{\text{Pos}}} \widehat{\phi}^*\, j_{\text{Pos}}\, \mathrm{d}V = 0\,,
\end{aligned} \tag{A.4a}$$

$$\begin{aligned}
&\frac{RT\,\kappa_{\text{Neg}}}{(D_{\text{Li}^+} + D_{\text{X}^-})\, F^2\, c_{\text{ref}}\, l_{\text{ref}}} \int_{V_{\text{Neg}}} \nabla\widehat{\phi}^* \cdot \nabla\phi^*\, \mathrm{d}V \\
&\quad + \frac{1}{(D_{\text{Li}^+} + D_{\text{X}^-})\, F\, c_{\text{ref}}\, l_{\text{ref}}} \int_{\partial V_{\text{Neg}} \cap \partial V_{\text{cc}}} \widehat{\phi}^*\, j_{\text{Neg cc}}\, \mathrm{d}V \\
&\quad + \frac{1}{(D_{\text{Li}^+} + D_{\text{X}^-})\, F\, c_{\text{ref}}\, l_{\text{ref}}} \int_{\partial V_{\text{SPE}} \cap \partial V_{\text{Neg}}} \widehat{\phi}^*\, j_{\text{Neg}}\, \mathrm{d}V = 0,
\end{aligned} \tag{A.4b}$$

$$\begin{aligned}
&\frac{1}{l_{\text{ref}}} \int_{V_{\text{SPE}}} \nabla\widehat{\phi}^* \cdot c^*\, \nabla\phi^*\, \mathrm{d}V - \frac{D_{\text{X}^-} - D_{\text{Li}^+}}{D_{\text{X}^-} + D_{\text{Li}^+}} \frac{1}{l_{\text{ref}}} \int_{V_{\text{SPE}}} \nabla\widehat{\phi}^* \cdot \nabla c^*\, \mathrm{d}V \\
&\quad - \frac{D_{\text{X}^-}}{D_{\text{Li}^+} + D_{\text{X}^-}} \left(\frac{\Omega_{\text{X}^-}}{\Omega} - \frac{D_{\text{Li}^+}}{D_{\text{X}^-}} \left(1 - \frac{\Omega_{\text{X}^-}}{\Omega} \right) \right) \frac{1}{l_{\text{ref}}} \int_{V_{\text{SPE}}} \nabla\widehat{\phi}^* \cdot c^*\, \nabla p^*\, \mathrm{d}V \\
&\quad + \frac{1}{(D_{\text{Li}^+} + D_{\text{X}^-})\, F\, c_{\text{ref}}\, l_{\text{ref}}} \int_{\partial V_{\text{SPE}} \cap \partial V_{\text{Pos}}} \widehat{\phi}^*\, j_{\text{Pos}}\, \mathrm{d}V \\
&\quad - \frac{1}{(D_{\text{Li}^+} + D_{\text{X}^-})\, F\, c_{\text{ref}}\, l_{\text{ref}}} \int_{\partial V_{\text{SPE}} \cap \partial V_{\text{Neg}}} \widehat{\phi}^*\, j_{\text{Neg}}\, \mathrm{d}V = 0,
\end{aligned} \tag{A.4c}$$

$$\begin{aligned}
&\frac{\Delta t}{l_{\text{ref}}^3} \int_{V_{\text{SPE}}} \widehat{c}^* \frac{\partial c^*}{\partial t}\, \mathrm{d}V + \frac{D\,\Delta t}{l_{\text{ref}}^3} \int_{V_{\text{SPE}}} \nabla\widehat{c}^* \cdot \nabla c^*\, \mathrm{d}V + \frac{1}{2} \frac{D\,\Delta t}{l_{\text{ref}}^3} \int_{V_{\text{SPE}}} \nabla\widehat{c}^* \cdot c^*\, \nabla p^*\, \mathrm{d}V \\
&\quad + \frac{\beta}{(D_{\text{Li}^+} + D_{\text{X}^-})\, F\, c_{\text{ref}}\, l_{\text{ref}}} \int_{\partial V_{\text{SPE}} \cap \partial V_{\text{Pos}}} \widehat{c}^*\, j_{\text{Pos}}\, \mathrm{d}V \\
&\quad - \frac{\beta}{(D_{\text{Li}^+} + D_{\text{X}^-})\, F\, c_{\text{ref}}\, l_{\text{ref}}} \int_{\partial V_{\text{SPE}} \cap \partial V_{\text{Neg}}} \widehat{c}^*\, j_{\text{Neg}}\, \mathrm{d}V = 0,
\end{aligned} \tag{A.4d}$$

$$\begin{aligned}
&\frac{1}{K\, l_{\text{ref}}} \int_{V_{\text{SPE}}} \widehat{\boldsymbol{\varepsilon}}^* : \mathbf{D}\boldsymbol{\varepsilon}^*\, \mathrm{d}V - \frac{\Omega\, c_{\text{ref}}}{l_{\text{ref}}^2} K\Omega \int_{V_{\text{SPE}}} \mathrm{tr}\,\widehat{\boldsymbol{\varepsilon}}^* \left(c^* - \frac{c^0}{c_{\text{ref}}} \right) \mathrm{d}V \\
&\quad - \frac{1}{K\, l_{\text{ref}}^2} \int_{V_{\text{SPE}}} \widehat{\boldsymbol{u}}^* \cdot \boldsymbol{t}\, \mathrm{d}V = 0,
\end{aligned} \tag{A.4e}$$

$$\begin{aligned}
&\frac{1}{l_{\text{ref}}^3} \int_{V_{\text{SPE}}} \widehat{p}^*\, p^*\, \mathrm{d}V + \frac{\Omega\, K}{RT\, l_{\text{ref}}^3} \int_{V_{\text{SPE}}} \widehat{p}^*\, \mathrm{tr}\,\widehat{\boldsymbol{\varepsilon}}^*\, \mathrm{d}V \\
&\quad - \frac{\Omega^2\, K c_{\text{ref}}}{RT\, l_{\text{ref}}^3} \int_{V_{\text{SPE}}} \widehat{p}^* \left(c^* - \frac{c^0}{c_{\text{ref}}} \right) \mathrm{d}V = 0,
\end{aligned} \tag{A.4f}$$

with

$$\beta = \frac{D_{\text{X}^-}\, \Delta t}{l_{\text{ref}}^2}\,. \tag{A.5}$$

A backward-Euler integration scheme is used to transform the time-continuum system of equation (A.4) into its incremental counterpart. A standard finite element approximation is adopted for the spatial discretization of the problem, after which the problem reduces to finding the vector of nodal unknowns $\mathbf{a}_{n+1} = \{\boldsymbol{\phi}_{n+1},\, \mathbf{c}_{n+1},\, \mathbf{u}_{n+1},\, \mathbf{p}_{n+1}\}$ at time t_{n+1} such that the incremental finite element equation

$$\mathbf{r}(\mathbf{a}_{n+1}) \equiv \mathbf{f}^{\,\text{int}}(\mathbf{a}_{n+1}) \;-\; \mathbf{f}_{n+1}^{\text{ext}} = \mathbf{0}\,, \tag{A.6}$$

is satisfied.

At each iteration k of the Newton-Raphson iterative scheme, the linear system of equations

$$\mathbf{K}\, \delta\mathbf{a}^k \;=\; -\mathbf{r}^{\,k-1} \tag{A.7}$$

is solved for $\delta\mathbf{a}^k$ where the residual vector

$$\mathbf{r}^{\,k-1} \equiv \mathbf{f}^{\,\text{int}}\left(\mathbf{a}_{n+1}^{k-1} \right) \;-\; \mathbf{f}_{n+1}^{\text{ext}} \tag{A.8}$$

and the global tangent matrix

$$\mathbf{K} \;=\; \left. \frac{\partial \mathbf{r}}{\partial \mathbf{a}_{n+1}} \right|_{\mathbf{a}_{n+1}^{k-1}}\,. \tag{A.9}$$

The vector of external forces $\mathbf{f}^{\text{ext}}$ (A.8) is identically equal to zero because only Dirichlet boundary conditions are considered in the numerical examples (refer to Section 4 for details), and thus $j_{\text{Pos cc}} = j_{\text{Neg cc}} = 0$ and $\boldsymbol{t} = \mathbf{0}$. The solution $\delta\mathbf{a}^k$ of the linear system (A.7) is applied to correct the vector of nodal unknowns

$$\mathbf{a}_{n+1}^k \;=\; \mathbf{a}_{n+1}^{k-1} \;+\; \delta\mathbf{a}^k\,. \tag{A.10}$$

The subscript $n+1$ and superscript $k-1$ emphasize that the nodal values refer to time step t_{n+1} at the $k-1$-th iteration. Details about iterative schemes for the solution of nonlinear initial boundary value problems can be found for example in Ref. [57].

Explicit expressions for the tangent matrices and residual vectors for the Newton-Raphson iteration scheme (A.7) computed at the element level are provided in Appendix A.1. Details about the numerical treatment of the interactions between different domains are provided in Appendix A.2.

Appendix A.1. Element level implementation

Attention is restricted in this section to the formulation of quantities at the element level. Expressions of nodal vectors and operators employed in the numerical implementation are provided. The dimensionless nodal quantities are collected into vectors as

$$\boldsymbol{\phi}_{n+1}^{k-1} = \left[\phi^{*\,(1)} \quad \dots \quad \phi^{*\,(n)}\right]^T, \tag{A.11a}$$

$$\mathbf{c}_{n+1}^{k-1} = \left[c^{*\,(1)} \quad \dots \quad c^{*\,(n)}\right]^T, \tag{A.11b}$$

$$\mathbf{u}_{n+1}^{k-1} = \left[u_x^{*\,(1)} \quad u_y^{*\,(1)} \quad \dots \quad u_x^{*\,(n)} \quad u_y^{*\,(n)}\right]^T, \tag{A.11c}$$

$$\mathbf{p}_{n+1}^{k-1} = \left[p^{*\,(1)} \quad \dots \quad p^{*\,(n)}\right]^T, \tag{A.11d}$$

and the same holds for the initial condition

$$\mathbf{c}^0 = \frac{c^0}{c_{\text{ref}}}\left[1^{(1)} \quad \dots \quad 1^{(n)}\right]^T, \tag{A.12}$$

where $n+1$ and $k-1$ have the same meaning as in Eq. (A.10) and (i) indicates the i-th node of an element with n nodes. The array

$$\mathbf{N} = \left[N^{(1)} \quad \dots \quad N^{(n)}\right] \tag{A.13}$$

collects the nodal shape functions of the finite element. In a two-dimensional context, the differential operators are grouped into the discrete symmetric gradient

$$\mathbf{B} = \begin{bmatrix} \frac{\partial N^{(1)}}{\partial x} & 0 & \dots & \frac{\partial N^{(n)}}{\partial x} & 0 \\ 0 & \frac{\partial N^{(1)}}{\partial y} & \dots & 0 & \frac{\partial N^{(n)}}{\partial y} \\ \frac{\partial N^{(1)}}{\partial y} & \frac{\partial N^{(1)}}{\partial x} & \dots & \frac{\partial N^{(n)}}{\partial y} & \frac{\partial N^{(n)}}{\partial x} \end{bmatrix}, \tag{A.14}$$

the discrete gradient operator

$$\mathbf{B}_{\text{grad}} = \begin{bmatrix} \frac{\partial N^{(1)}}{\partial x} & \dots & \frac{\partial N^{(n)}}{\partial x} \\ \frac{\partial N^{(1)}}{\partial y} & \dots & \frac{\partial N^{(n)}}{\partial y} \end{bmatrix}, \tag{A.15}$$

and the discrete trace operator

$$\mathbf{B}_{\text{trace}} = \left[\frac{\partial N^{(1)}}{\partial x} \quad \frac{\partial N^{(1)}}{\partial y} \quad \dots \quad \frac{\partial N^{(n)}}{\partial x} \quad \frac{\partial N^{(n)}}{\partial y}\right]. \tag{A.16}$$

Electrode elements. The element tangent matrix and the residual vector referring to the electrodes are expressed as

$$\mathbf{K}_e^{\phi\phi} = \frac{RT\,\kappa_{\text{el}}}{(D_{\text{Li}^+} + D_{\text{X}^-})c_{\text{ref}}\,F^2\,l_{\text{ref}}} \int_{V_{\text{el}\,e}} \mathbf{B}_{\text{grad}}^T\,\mathbf{B}_{\text{grad}}\,\mathrm{d}V, \tag{A.17}$$

$$\mathbf{r}_e^{\phi} = \frac{RT\,\kappa_{\text{el}}}{(D_{\text{Li}^+} + D_{\text{X}^-})\,c_{\text{ref}}\,F^2\,l_{\text{ref}}} \int_{V_{\text{el}\,e}} \mathbf{B}_{\text{grad}}^T\,\mathbf{B}_{\text{grad}}\,\boldsymbol{\phi}\,\mathrm{d}V. \tag{A.18}$$

Vector $\boldsymbol{\phi}$ refers to time step t_{n+1} and iteration $k-1$, subscript $n+1$ and superscript $k-1$ are omitted to favor readability.

Solid polymer electrolyte elements. The contributions to the element tangent matrix and the residual vector that follow from the space-time discretization of equation (9) read

$$\begin{aligned}
\mathbf{K}_e^{\phi\phi} &= \frac{1}{l_{\text{ref}}} \int_{V_{\text{SPE}\,e}} \mathbf{B}_{\text{grad}}^T\,\mathbf{B}_{\text{grad}}\,\mathbf{N}\,\mathbf{c}\,\mathrm{d}V, \\
\mathbf{K}_e^{\phi c} &= \frac{1}{l_{\text{ref}}} \int_{V_{\text{SPE}\,e}} \mathbf{B}_{\text{grad}}^T\,\mathbf{B}_{\text{grad}}\boldsymbol{\phi}\,\mathbf{N}\,\mathrm{d}V \\
&\quad -\frac{D_{\text{X}^-} - D_{\text{Li}^+}}{D_{\text{Li}^+} + D_{\text{X}^-}} \frac{1}{l_{\text{ref}}} \int_{V_{\text{SPE}\,e}} \mathbf{B}_{\text{grad}}^T\,\mathbf{B}_{\text{grad}}\,\mathrm{d}V \\
&\quad -c_1 \int_V \mathbf{B}_{\text{grad}}^T\,\mathbf{B}_{\text{grad}}\,\mathbf{p}\,\mathbf{N}\,\mathrm{d}V, \\
\mathbf{K}_e^{\phi p} &= -c_1 \int_{V_{\text{SPE}\,e}} \mathbf{B}_{\text{grad}}^T\,\mathbf{B}_{\text{grad}}\,\mathbf{N}\,\mathbf{c}\,\mathrm{d}V, \\
\mathbf{K}_e^{cc} &= \frac{1}{l_{\text{ref}}^3} \int_{V_{\text{SPE}\,e}} \mathbf{N}^T\,\mathbf{N}\,\mathrm{d}V + \frac{D\,\Delta t}{l_{\text{ref}}^3} \int_{V_{\text{SPE}\,e}} \mathbf{B}_{\text{grad}}^T\,\mathbf{B}_{\text{grad}}\,\mathrm{d}V \\
&\quad + \frac{1}{2}\,\frac{D\,\Delta t}{l_{\text{ref}}^3} \int_{V_{\text{SPE}\,e}} \mathbf{B}_{\text{grad}}^T\,\mathbf{B}_{\text{grad}}\,\mathbf{p}\,\mathbf{N}\,\mathrm{d}V, \\
\mathbf{K}_e^{cp} &= \frac{1}{2}\,\frac{D\,\Delta t}{l_{\text{ref}}^3} \int_{V_{\text{SPE}\,e}} \mathbf{B}_{\text{grad}}^T\,\mathbf{B}_{\text{grad}}\,\mathbf{N}\,\mathbf{c}\,\mathrm{d}V, \\
\mathbf{K}_e^{uu} &= \frac{1}{K\,l_{\text{ref}}} \int_{V_{\text{SPE}\,e}} \mathbf{B}^T\,\mathbf{D}\,\mathbf{B}\,\mathrm{d}V, \\
\mathbf{K}_e^{uc} &= -\frac{\Omega\,c_{\text{ref}}}{l_{\text{ref}}^2} \int_{V_{\text{SPE}\,e}} \mathbf{B}_{\text{trace}}^T\,\mathbf{N}\,\mathrm{d}V, \\
\mathbf{K}_e^{pp} &= \frac{1}{l_{\text{ref}}^3} \int_{V_{\text{SPE}\,e}} \mathbf{N}^T\,\mathbf{N}\,\mathrm{d}V, \\
\mathbf{K}_e^{pu} &= \frac{\Omega\,K}{RT\,l_{\text{ref}}^2} \int_{V_{\text{SPE}\,e}} \mathbf{N}^T\,\mathbf{B}_{\text{trace}}\,\mathrm{d}V, \\
\mathbf{K}_e^{pc} &= -\frac{\Omega^2\,K\,c_{\text{ref}}}{RT\,l_{\text{ref}}^3} \int_{V_{\text{SPE}\,e}} \mathbf{N}^T\,\mathbf{N}\,\mathrm{d}V,
\end{aligned} \tag{A.19}$$

with

$$c_1 = \frac{D_{\text{X}^-}}{D_{\text{Li}^+} + D_{\text{X}^-}} \left(\frac{\Omega_{\text{X}^-}}{\Omega} - \frac{D_{\text{Li}^+}}{D_{\text{X}^-}}\left(1 - \frac{\Omega_{\text{X}^-}}{\Omega}\right)\right) \frac{1}{l_{\text{ref}}}$$

$$
\begin{aligned}
\mathbf{r}_e^{\phi} &= \frac{1}{l_{\text{ref}}} \int_{V_{\text{SPE}\,e}} \mathbf{B}_{\text{grad}}^T \, \mathbf{B}_{\text{grad}} \, \boldsymbol{\phi} \, \mathbf{N} \, \mathbf{c} \, dV \\
&\quad - \frac{D_{\text{X}^-} - D_{\text{Li}^+}}{(D_{\text{Li}^+} + D_{\text{X}^-})\, l^*} \int_{V_{\text{SPE}\,e}} \mathbf{B}_{\text{grad}}^T \, \mathbf{B}_{\text{grad}} \, \mathbf{c} \, dV \\
&\quad - c_1 \int_{V_{\text{SPE}\,e}} \mathbf{B}_{\text{grad}}^T \, \mathbf{B}_{\text{grad}} \, \mathbf{p} \, \mathbf{N} \, \mathbf{c} \, dV, \\
\mathbf{r}_e^{c} &= \frac{1}{l_{\text{ref}}^3} \int_{V_{\text{SPE}\,e}} \mathbf{N}^T \, \mathbf{N} \, \Delta\mathbf{c} \, dV \\
&\quad + \frac{D\,\Delta t}{l_{\text{ref}}^3} \int_{V_{\text{SPE}\,e}} \mathbf{B}_{\text{grad}}^T \, \mathbf{B}_{\text{grad}} \, \mathbf{c} \, dV \\
&\quad + \frac{1}{2} \frac{D\,\Delta t}{l_{\text{ref}}^3} \int_{V_{\text{SPE}\,e}} \mathbf{B}_{\text{grad}}^T \, \mathbf{B}_{\text{grad}} \, \mathbf{p} \, \mathbf{N} \, \mathbf{c} \, dV \,, \\
\mathbf{r}_e^{u} &= \frac{1}{K\, l^*} \int_{V_{\text{SPE}\,e}} \mathbf{B}^T \, \mathbf{D} \, \mathbf{B} \, \mathbf{u} \, dV \\
&\quad - \frac{\Omega\, c_{\text{ref}}}{l_{\text{ref}}^2} \int_{V_{\text{SPE}\,e}} \mathbf{B}_{\text{trace}}^T \, \mathbf{N} \Big(\mathbf{c} - \mathbf{c}^0 \Big) \, dV, \\
\mathbf{r}_e^{p} &= \frac{1}{l_{\text{ref}}^3} \int_{V_{\text{SPE}\,e}} \mathbf{N}^T \, \mathbf{N} \, \mathbf{p} \, dV \\
&\quad + \frac{\Omega\, K}{RT\, l_{\text{ref}}^2} \int_{V_{\text{SPE}\,e}} \mathbf{N}^T \, \mathbf{B}_{\text{trace}} \, \mathbf{u} \, dV \\
&\quad - \frac{\Omega^2\, K\, c_{\text{ref}}}{RT\, l_{\text{ref}}^3} \int_{V_{\text{SPE}\,e}} \mathbf{N}^T \, \mathbf{N} \Big(\mathbf{c} - \mathbf{c}^0 \Big) \, dV \,,
\end{aligned}
\tag{A.20}
$$

where the incremental concentration is defined as

$$
\Delta\mathbf{c} = \mathbf{c} - \mathbf{c}_n \,, \tag{A.21}
$$

being $\mathbf{c}_n$ the vector containing the converged solution for (A.11b) at the previous time increment t_n. The elastic stiffness matrix for plane strain conditions reads

$$
\mathbf{D} = \frac{E}{(1+\nu)(1-2\,\nu)} \begin{bmatrix} 1-\nu & \nu & \nu & 0 \\ \nu & 1-\nu & \nu & 0 \\ \nu & \nu & 1-\nu & 0 \\ 0 & 0 & 0 & \frac{1}{2}-\nu \end{bmatrix} . \tag{A.22}
$$

Vectors $\boldsymbol{\phi}$, $\mathbf{c}$, $\Delta\mathbf{c}$, $\mathbf{u}$ and $\mathbf{p}$ refer to time step t_{n+1} and iteration $k-1$, subscript $n+1$ and superscript $k-1$ are omitted to favor readability.

The element tangent matrix and the residual vector assembled for each solid polymer electrolyte element read

$$
\mathbf{K}_e = \begin{bmatrix} \mathbf{K}_e^{\phi\phi} & \mathbf{K}_e^{\phi c} & 0 & \mathbf{K}_e^{\phi p} \\ 0 & \mathbf{K}_e^{cc} & 0 & \mathbf{K}_e^{cp} \\ 0 & \mathbf{K}_e^{uc} & \mathbf{K}_e^{uu} & 0 \\ 0 & \mathbf{K}_e^{pc} & \mathbf{K}_e^{pu} & \mathbf{K}_e^{pp} \end{bmatrix}, \quad \mathbf{r}_e = \begin{bmatrix} \mathbf{r}_e^{\phi} \\ \mathbf{r}_e^{c} \\ \mathbf{r}_e^{u} \\ \mathbf{r}_e^{p} \end{bmatrix} . \tag{A.23}
$$

Appendix A.2. Global system of equations and Lagrange multipliers

To address the interface conditions (12) and (13), electrodes and SPE are meshed as three independent domains. Couples of nodes with the same coordinates are generated along the electrode-electrolyte interface $\partial V_{\text{el}} \cap \partial V_{\text{SPE}}$. For any l-th couple of nodes a Lagrange multiplier $\lambda^{(l)}$ is introduced among the unknowns $\mathbf{a}$, representing the contribution of the integral

$$
\frac{1}{(D_{\text{Li}^+} + D_{\text{X}^-})\, F\, c_{\text{ref}}\, l_{\text{ref}}} \int\limits_{\partial V_{\text{SPE}} \cap \partial V_{\text{el}}} \widehat{\phi}^{\,*} \, j_{\text{el}} \; dV \,, \tag{A.24}
$$

appearing in (A.4a-c), restricted to the area of influence of the corresponding l-th couple. The total number of Lagrange multipliers equals the number of nodes that lie along the two electrode-SPE interfaces N_{int}.

The complete set of unknowns, the global tangent matrix and residual vector for the three domains can be expressed as follows:

$$
\delta a = \begin{bmatrix} \delta\boldsymbol{\phi}_{\text{Pos}} \\ \delta\boldsymbol{\phi}_{\text{SPE}} \\ \delta\mathbf{c}_{\text{SPE}} \\ \delta\mathbf{u}_{\text{SPE}} \\ \delta\mathbf{p}_{\text{SPE}} \\ \delta\boldsymbol{\phi}_{\text{Neg}} \\ \delta\boldsymbol{\lambda} \end{bmatrix}, \quad \mathbf{r} = \begin{bmatrix} \mathbf{r}_{\text{Pos}}^{\phi} - \boldsymbol{\lambda}_{\text{Pos}}^{k-1} \\ \mathbf{r}_{\text{SPE}}^{\phi} + \boldsymbol{\lambda}_{\text{Pos}}^{k-1} + \boldsymbol{\lambda}_{\text{Neg}}^{k-1} \\ \mathbf{r}_{\text{SPE}}^{c} + \beta \left(\boldsymbol{\lambda}_{\text{Pos}}^{k-1} + \boldsymbol{\lambda}_{\text{Neg}}^{k-1} \right) \\ \mathbf{r}_{\text{SPE}}^{u} \\ \mathbf{r}_{\text{SPE}}^{p} \\ \mathbf{r}_{\text{Neg}}^{\phi} - \boldsymbol{\lambda}_{\text{Neg}}^{k-1} \\ \mathbf{r}^{\lambda} \end{bmatrix},
$$

$$
\mathbf{K} = \begin{bmatrix} \mathbf{K}_{\text{Pos}}^{\phi\phi} & 0 & 0 & 0 & 0 & 0 & \mathbf{C}_{\text{Pos}}^T \\ 0 & \mathbf{K}_{\text{SPE}}^{\phi\phi} & \mathbf{K}_{\text{SPE}}^{\phi c} & 0 & \mathbf{K}_{\text{SPE}}^{\phi p} & 0 & \mathbf{C}_{\text{SPE}}^T \\ 0 & 0 & \mathbf{K}_{\text{SPE}}^{cc} & 0 & \mathbf{K}_{\text{SPE}}^{cp} & 0 & \beta\, \mathbf{C}_{\text{SPE}}^T \\ 0 & 0 & \mathbf{K}_{\text{SPE}}^{uc} & \mathbf{K}_{\text{SPE}}^{uu} & 0 & 0 & 0 \\ 0 & 0 & \mathbf{K}_{\text{SPE}}^{pc} & \mathbf{K}_{\text{SPE}}^{pu} & \mathbf{K}_{\text{SPE}}^{pp} & 0 & 0 \\ 0 & 0 & 0 & 0 & 0 & \mathbf{K}_{\text{Neg}}^{\phi\phi} & \mathbf{C}_{\text{Neg}}^T \\ \mathbf{C}_{\text{Pos}} & \mathbf{C}_{\text{SPE}} & 0 & 0 & 0 & \mathbf{C}_{\text{Neg}} & 0 \end{bmatrix} \tag{A.25}
$$

where the matrices $\mathbf{K}_{\text{Pos}}^{\phi\phi}$ and $\mathbf{K}_{\text{Neg}}^{\phi\phi}$ represent the element tangent matrices $\mathbf{K}_{\text{el}}^{\phi\phi}$ (A.17) assembled over the positive and negative electrodes domains, respectively, while each matrix $\mathbf{K}_{\text{SPE}}^{mn}$ collects the contributions of the corresponding element tangent matrices $\mathbf{K}_{\text{el}}^{mn}$ (A.19) assembled over the SPE domain. This representation is chosen to emphasize the relationship established through the Lagrange multipliers between nodal quantities that belong to different domains.

The relationship between electrostatic potentials (11) and continuity of the current density (12) is enforced between couples of nodes along the interface through the constraint matrices $\mathbf{C}$ and the Lagrange multipliers $\boldsymbol{\lambda} = \left\{ \lambda^{(1)}, \ldots, \lambda^{(N_{\text{int}})} \right\}$. In Eq. (A.25), the matrices referring to both interfaces are collected into $\mathbf{C}_{\text{SPE}} = \mathbf{C}_{\text{SPE Pos}} + \mathbf{C}_{\text{SPE Neg}}$ for the SPE, and $\delta\boldsymbol{\lambda}$ represents the correction corresponding to the Lagrange multipliers during the Newton-Raphson procedure (A.7).

The contribution of terms (A.24) computed at the previous iterations of the Newton-Raphson is collected in vectors $\boldsymbol{\lambda}_{\text{Pos}}^{k-1}$ and $\boldsymbol{\lambda}_{\text{Neg}}^{k-1}$ (the subscripts emphasize that different Lagrange multiplies apply at the two interfaces). Since $\widehat{\phi}^{\,*}$ and $\widehat{c}^{\,*}$ are mere test functions, the terms in equations (A.4c) and (A.4d) along the interface $\partial V_{\text{SPE}} \cap \partial V_{\text{el}}$ only differ by factor β that links the charge and mass conversion equations. The charge-mass conversion (13) enters into the mass conservation equation of the system (A.25) through $\beta\, \mathbf{C}_{\text{SPE}}^T$ and $\beta \left(\boldsymbol{\lambda}_{\text{Pos}}^{k-1} + \boldsymbol{\lambda}_{\text{Neg}}^{k-1} \right)$.

References

[1] L. Long, S. Wang, M. Xiao, Y. Meng, Polymer electrolytes for lithium polymer batteries, J. Mater. Chem. A 4 (2016) 10038–10069.
[2] J. Long, B. Dunn, D. Rolison, H. White, Three-dimensional battery architectures, Chem. Rev. 104 (10) (2004) 4463–4492.
[3] B. Dunn, J. Long, D. Rolison, Rethinking multifunction in three dimensions for miniaturizing electrical energy storage, Electrochem. Soc. Interface 17 (3) (2008) 49–53.
[4] J. Snyder, R. Carter, E. Wetzel, Electrochemical and mechanical behavior in mechanically robust solid polymer electrolytes for use in multifunctional structural batteries, Chem. Mater. 19 (2007) 3793–3801.
[5] P. Liu, E. Sherman, A. Jacobsen, Design and fabrication of multifunctional structural batteries, J. Power Sources 189 (2009) 646–650.
[6] K. Murata, S. Izuchi, Y. Yoshihisa, An overview of the research and development of solid polymer electrolyte batteries, Electrochim. Acta 45 (8) (2000) 1501–1508.
[7] K. Edström, D. Brandell, T. Gustafsson, L. Nyholm, Electrodeposition as a tool for 3D microbattery fabrication, Electrochem. Soc. Interface 20 (2) (2011) 41–46.
[8] D. Hallinan Jr., N. Balsara, Polymer electrolytes, Annu. Rev. Mater. Res. 43 (1) (2013) 503–525.
[9] G. Bucci, Y.-M. Chiang, W. Carter, Formulation of the coupled electrochemical-mechanical boundary-value problem, with applications to transport of multiple charged species, Acta Mater. 104 (2016) 33–51.
[10] X. Su, K. Guo, T. Ma, P. Tamirisa, H. Ye, H. Gao, B. Sheldon, Deformation and chemomechanical degradation at solid electrolyte-electrode interfaces, ACS Energy Lett. 2 (8) (2017) 1729–1733.
[11] S. Audet, J. Carney, G. Haubrich, D. Ruben, E. Herrmann, V. Larik, R. Receveur, E. Scott, G. Vaughn, 3.14 - medical applications, in: Y. Gianchandani, O. Tabata, H. Zappe (Eds.), Reference Module in Materials Science and Materials Engineering, from Comprehensive Microsystems, Elsevier, Oxford, 2008, pp. 421–474.
[12] A. Teo, A. Mishra, I. Park, Y. Kim, W. Park, Y. Yoon, Polymeric biomaterials for medical implants and devices, ACS Biomater. Sci. Eng. 2 (4) (2016) 454–472.
[13] X. Wei, J. Liu, Power sources and electrical recharging strategies for implantable medical devices, Front. Energy Power Eng. China 2 (1) (2008) 1–13.
[14] N. Cirigliano, G. Sun, D. Membreno, P. Malati, C. Kim, B. Dunn, 3D architectured anodes for lithium-ion microbatteries with large areal capacity, Energy Technol. 2 (4) (2014) 362–369.
[15] A. Talin, D. Ruzmetov, A. Kolmakov, K. McKelvey, N. Ware, F. El Gabaly, B. Dunn, H. White, Fabrication, testing, and simulation of all-solid-state three-dimensional Li-ion batteries, ACS Appl. Mater. Interfaces 8 (47) (2016) 32385–32391.
[16] R.W. Hart, H.S. White, B. Dunn, D.R. Rolison, 3-D microbatteries, Electrochem. Commun. 5 (2) (2003) 120–123.
[17] V. Zadin, H. Kasemägi, A. Aabloo, D. Brandell, Modelling electrode material utilization in the trench model 3D-microbattery by finite element analysis, J. Power Sources 195 (18) (2010) 6218–6224.
[18] V. Zadin, D. Brandell, H. Kasemägi, A. Aabloo, J. Thomas, Finite element modelling of ion transport in the electrolyte of a 3D-microbattery, Solid State Ionics 192 (1) (2011) 279–283.
[19] V. Zadin, D. Brandell, Modelling polymer electrolytes for 3D-microbatteries using finite element analysis, Electrochim. Acta 57 (2011) 237–243.
[20] V. Zadin, D. Brandell, H. Kasemägi, J. Lellep, A. Aabloo, Designing the 3D-microbattery geometry using the level-set method, J. Power Sources 244 (2013) 417–428.
[21] P. Priimägi, D. Brandell, S. Srivastav, A. Aabloo, H. Kasemägi, V. Zadin, Optimizing the design of 3D-pillar microbatteries using finite element modelling, Electrochim. Acta 209 (2016) 138–148.
[22] P. Priimägi, H. Kasemägi, A. Aabloo, D. Brandell, V. Zadin, Thermal simulations of polymer electrolyte 3D Li-microbatteries, Electrochim. Acta 244 (2017) 129–138.
[23] D. Grazioli, M. Magri, A. Salvadori, Computational modeling of Li-ion batteries, Comput. Mech. 58 (6) (2016) 889–909.
[24] P.P. Natsiavas, K. Weinberg, D. Rosato, M. Ortiz, Effect of prestress on the stability of electrode-electrolyte interfaces during charging in lithium batteries, J. Mech. Phys. Solid. 95 (2016) 92–111.
[25] D. Grazioli, O. Verners, V. Zadin, D. Brandell, A. Simone, Electrochemical-mechanical modeling of solid polymer electrolytes: Impact of mechanical stresses on Li-ion battery performance, Electrochim. Acta 296 (2019) 1122–1141, https://doi.org/10.1016/j.electacta.2018.07.234.
[26] X. Su, T. Zhang, X. Liang, H. Gao, B. Sheldon, Employing nanoscale surface morphologies to improve interfacial adhesion between solid electrolytes and Li ion battery cathodes, Acta Mater. 98 (2015) 175–181.
[27] A. Salvadori, D. Grazioli, M. Geers, D. Danilov, P. Notten, A multiscale-compatible approach in modeling ionic transport in the electrolyte of (lithium ion) batteries, J. Power Sources 293 (2015) 892–911.
[28] A. Salvadori, D. Grazioli, M. Magri, M. Geers, D. Danilov, P. Notten, On the role of saturation in modeling ionic transport in the electrolyte of (lithium ion) batteries, J. Power Sources 294 (2015) 696–710.
[29] D. Danilov, P.H.L. Notten, Mathematical modelling of ionic transport in the electrolyte of Li-ion batteries, Electrochim. Acta 53 (17) (2008) 5569–5578.
[30] J. Newman, K. Thomas-Alyea, Electrochemical Systems, third ed., John Wiley and Sons, 2004.
[31] E. Asp, Multifunctional composite materials for energy storage in structural load paths, Plast. Rubber Compos. 42 (4) (2013) 144–149.
[32] C. Zhuang, Z. Xiong, H. Ding, A level set method for topology optimization of heat conduction problem under multiple load cases, Comput. Meth. Appl. Mech. Eng. 196 (2007) 1074–1084.
[33] L. Baggetto, R. Niessen, F. Roozeboom, P. Notten, High energy density all-solid-state batteries: A challenging concept towards 3D integration, Adv. Funct. Mater. 18 (2008) 1057–1066.
[34] A. Westover, F. Shabab, J. Tian, S. Bernath, L. Oakes, W. Erwin, R. Carter, R. Bardhan, C. Pint, Stretching ion conducting polymer electrolytes: In-situ correlation of mechanical, ionic transport, and optical properties, J. Electrochem. Soc. 161 (6) (2014) E112–E117.
[35] T. Kelly, B. Ghadi, S. Berg, H. Ardebili, In situ study of strain-dependent ion conductivity of stretchable polyethylene oxide electrolyte, Sci. Rep. 6 (2016) 20128.
[36] M. Moreno, R. Quijada, M.S. Ana, E. Benavente, P. Gomez-Romero, G. González, Electrical and mechanical properties of poly(ethylene oxide)/intercalated clay polymer electrolyte, Electrochim. Acta 58 (2011) 112–118.
[37] A. Amirsadeghi, J. Lee, S. Park, A simulation study on the effect of cross-linking agent concentration for defect tolerant demolding in UV nanoimprint lithography, Langmuir 28 (31) (2012) 11546–11554.
[38] Y. Gan, J. Yin, X. Jiang, Self-wrinkling induced by the photopolymerization and self-assembly of fluorinated polymer at air/liquid interface, J. Mater. Chem. A 2 (43) (2014) 18574–18582.
[39] O. Verners, B. Thijsse, A. van Duin, A. Simone, Salt concentration effects on mechanical properties of $LiPF_6$/poly(propylene glycol) diacrylate solid electrolyte: Insights from reactive molecular dynamics simulations, Electrochim. Acta 221 (2016) 115–123.
[40] M. Qu, W. Woodford, J. Maloney, W. Carter, Y.-M. Chiang, K. Van Vliet, Nanomechanical quantification of elastic, plastic, and fracture properties of $LiCoO_2$, Adv. Energy Mater. 2 (8) (2012) 940–944.
[41] Y. Qi, L. Hector, C. James, K. Kim, Lithium concentration dependent elastic properties of battery electrode materials from first principles calculations, J. Electrochem. Soc. 161 (11) (2014) F3010–F3018.
[42] L. Wu, W. Lee, J. Zhang, First principles study on the electrochemical, thermal and mechanical properties of $LiCoO_2$ for thin film rechargeable battery, Mater. Today: Proc. 1 (1) (2014) 82–93.
[43] J.R. Cost, K.R. Janowski, R.C. Rossi, Elastic properties of isotropic graphite, Phil. Mag. 17 (148) (1968) 851–854.
[44] Y. Qi, H. Guo, L. Hector Jr., A. Timmons, Threefold increase in the Young's modulus of graphite negative electrode during lithium intercalation, J. Electrochem. Soc. 157 (5) (2010) A558–A566.
[45] H. Wang, Y. Jang, B. Huang, D. Sadoway, Y. Chiang, TEM study of electrochemical cycling-induced damage and disorder in $LiCoO_2$ cathodes for rechargeable lithium batteries, J. Electrochem. Soc. 146 (2) (1999) 473–480.
[46] T. Ohzuku, A. Ueda, Why transition metal (di)oxides are the most attractive materials for batteries, Solid State Ionics 69 (1994), 201–2011.
[47] R. Wartena, A. Curtright, C. Arnold, A. Piqué, K. Swider-Lyons, Li-ion microbatteries generated by a laser direct-write method, J. Power Sources 126 (1–2) (2004) 193–202.
[48] L. Le Van-Jodin, F. Ducroquet, F. Sabary, I. Chevalier, Dielectric properties, conductivity and Li^+ ion motion in LiPON thin films, Solid State Ionics 253 (2013) 151–156.
[49] M. Klett, M. Giesecke, A. Nyman, F. Hallberg, R. Lindström, G. Lindbergh, I. Furó, Quantifying mass transport during polarization in a Li ion battery electrolyte by in situ ^{7}Li NMR imaging, J. Am. Chem. Soc. 134 (36) (2012) 14654–14657.
[50] G. Bucci, T. Swamy, Y.-M. Chiang, W. Carter, Modeling of internal mechanical failure of all-solid-state batteries during electrochemical cycling, and implications for battery design, J. Mater. Chem. A 5 (2017) 19422–19430.
[51] G. Bucci, T. Swamy, Y.-M. Chiang, W. Carter, Random walk analysis of the effect of mechanical degradation on all-solid-state battery power, J. Electrochem. Soc. 164 (12) (2017) A2660–A2664.
[52] A. Mussa, M. Klett, G. Lindbergh, R. Lindström, Effects of external pressure on the performance and ageing of single-layer lithium-ion pouch cells, J. Power Sources 385 (2018) 18–26.
[53] J. Cannarella, C. Arnold, Stress evolution and capacity fade in constrained lithium-ion pouch cells, J. Power Sources 245 (2014) 745–751.
[54] V. Sethuraman, N.V. Winkle, D. Abraham, A. Bower, P. Guduru, Real-time stress measurements in lithium-ion battery negative-electrodes, J. Power Sources 206 (2012) 334–342.
[55] H. Ardebili, Private Communication, October 2017.
[56] A.F. Bower, P.R. Guduru, A simple finite element model of diffusion, finite deformation, plasticity and fracture in lithium ion insertion electrode materials, Model. Simulat. Mater. Sci. Eng. 20 (4) (2012), 045004.
[57] E. de Souza Neto, D. Perić, D. Owen, Computational Methods for Plasticity, first ed., Wiley, 2014.